

<b>REPORT DOCUMENTATION PAGE</b>			Form Approved OMB NO. 0704-0188	
Public reporting burden for this collection of information is estimated to average 1 hour per response, including the time for reviewing instructions, searching existing data sources, gathering and maintaining the data needed, and completing and reviewing the collection of information. Send comment regarding this burden estimate or any other aspect of this collection of information, including suggestions for reducing this burden, to Washington Headquarters Services, Directorate for Information Operations and Reports, 1215 Jefferson Davis Highway, Suite 1204, Arlington, VA 22202-4302, and to the Office of Management and Budget, Paperwork Reduction Project (0704-0188), Washington, DC 20503.				
1. AGENCY USE ONLY (Leave blank)		2. REPORT DATE June 30, 1998		3. REPORT TYPE AND DATES COVERED 7/1/97-6/30/98
4. TITLE AND SUBTITLE Investigation of Normal Incidence Absorption and Optical Gain in Multicolor and Simplified N-type Quantum Well Infrared Photodetectors			5. FUNDING NUMBERS  DAA655-97-1-0307	
6. AUTHOR(S) Sheng S. Li, Professor Xudong Jiang, Research Associate				
7. PERFORMING ORGANIZATION NAMES(S) AND ADDRESS(ES)  University of Florida Gainesville, FL 32611-6130			8. PERFORMING ORGANIZATION REPORT NUMBER	
9. SPONSORING / MONITORING AGENCY NAME(S) AND ADDRESS(ES)  U.S. Army Research Office P.O. Box 12211 Research Triangle Park., NC 27709-2211			10. SPONSORING / MONITORING AGENCY REPORT NUMBER  ARO 37278.3-EL	
11. SUPPLEMENTARY NOTES The views, opinions and/or findings contained in this report are those of the author(s) and should not be construed as an official Department of the Army position, policy or decision, unless so designated by other documentation.				
12a. DISTRIBUTION / AVAILABILITY STATEMENT  Approved for public release; distribution unlimited.			12 b. DISTRIBUTION CODE	
13. ABSTRACT (Maximum 200 words)  In this research project, we have conducted theoretical and experimental studies on normal incidence absorption in <i>n</i> -type direct gap QWIPs. A theoretical model for calculating the TE to TM transition ratios for the symmetrical LWIR- and step MWIR- QWIPs has been developed in this work. The role of strain on the normal incidence absorption has been investigated. We have also calculated the absorption coefficients for several <i>n</i> -type QWIPs, including both high -strain MWIR QWIP and LWIR TC-QWIPs. Analysis of simplified QWIPs for low photon background applications has been made. We have also studied the quantum confined Stark effect in a weakly coupled double quantum wells structure. Experimental study on three QWIP samples with different device structures, processing parameters and experimental conditions has been made to study the various effects on the normal incidence absorption. Several new simplified QWIPs have been designed and processed which show strong evidence of normal incidence absorption. Finally, a novel four-stack four-color QWIP has been designed, fabricated and characterized. Several journal and conference papers have been published and presented from this work.				
14. SUBJECT TERMS  <i>n</i> -type direct gap quantum well infrared photodetector (QWIP), normal incidence absorption, absorption coefficient, strain, multi-color, Stark effect			15. NUMBER OF PAGES	
			16. PRICE CODE	
17. SECURITY CLASSIFICATION OR REPORT UNCLASSIFIED	18. SECURITY CLASSIFICATION OF THIS PAGE UNCLASSIFIED	19. SECURITY CLASSIFICATION OF ABSTRACT UNCLASSIFIED	20. LIMITATION OF ABSTRACT  UL	

**INVESTIGATION OF NORMAL INCIDENCE ABSORPTION AND  
OPTICAL GAIN IN MULTICOLOR AND SIMPLIFIED N-TYPE  
QUANTUM WELL INFRARED PHOTODETECTORS**

**FINAL TECHNICAL REPORT**

(covering the period from July 1, 1997 to June 30, 1998)

Sheng S. Li, Professor  
Xudong Jiang, Research Associate

July 1, 1998

U.S. ARMY RESEARCH OFFICE

Dept. of Electrical and Computer Engineering  
University of Florida  
Gainesville, FL 32611-6130  
tex/fax: 352-392-4937  
email: shengli@eng.ufl.edu

APPROVED FOR PUBLIC RELEASE;  
DISTRIBUTION UNLIMITED.

THE VIEWS, OPINIONS, AND/OR FINDINGS CONTAINED IN THIS REPORT ARE  
THOSE OF THE AUTHOR(S) AND SHOULD NOT BE CONSTRUED AS AN  
OFFICIAL DEPARTMENT OF THE ARMY POSITION, POLICY, OR DECISION,  
UNLESS SO DESIGNATED BY OTHER DOCUMENTATION.

19981228 049

## TABLE OF CONTENTS

Summary .....	3
1. Theoretical Study of Normal Incidence Absorption in <i>n</i> -type Direct Gap QWIPs.....	4
1.1 Introduction.....	4
1.2 Summary of existing theories on normal incidence absorption mechanisms.....	5
1.2.1 One- band model considering spatial variation of effective mass .....	6
1.2.2 Kane Model .....	7
1.2.3 Multi-band coupling effects .....	8
1.3 Theoretical Study of Normal Incidence Absorption in <i>n</i> -type QWIPs.....	8
1.3.1 One- band model taking into account spatial variations of both the effective mass and refractive index .....	8
1.3.2 The role of strain on normal incidence absorption.....	15
1.4 Other possible normal incidence absorption mechanisms .....	16
1.4.1 Interface roughness.....	16
1.4.2 The effect of donor states .....	16
1.5 Conclusions.....	17
2. Intersubband Absorption Coefficient in QWIPs.....	21
3. Study of Normal Incidence Absorption in N-type QWIPs .....	25
3.1 Influence of experimental conditions on normal incidence absorption.....	25
3.2 Investigation of new S-QWIP structures .....	28
3.2.1 LWIR QWIP –A.....	29
3.2.2 MWIR QWIP- B and C .....	29
3.3 Normal incidence absorption in regular QWIPs and EQWIP.....	30
4. Simplified (S-) QWIPs for Low Temperature and Low Background Applications .....	44

4.1	Variation of Black Body Flux With Field of View Angle.....	44
4.2	Low Temperature and Low Background Modeling for the S-QWIP .....	44
5.	A Novel Four- Stack Four- Color QWIP for MWIR and LWIR Applications .....	52
5.1	Introduction.....	52
5.2	Device Performance and Characteristics .....	54
5.2.1	The top stack .....	54
5.2.2	The bottom stack .....	55
5.2.3	The MWIR-LWIR stacked QWIP .....	56
6.	Quantum Confined Stark Effect in an Asymmetric Weakly Coupled Double Quantum Wells Structure .....	70
6.1	Introduction.....	70
6.2	Formulation.....	71
6.3	Results and Discussion .....	75
6.3.1	Variation of energy levels and oscillators with structure parameters .....	75
6.3.2	The effect of electric field .....	77
6.3.3	Device performance.....	78
7.	Publications and technical reports .....	86
8.	References.....	87

## Summary

The objective of this research project is to investigate the anomalous normal incidence absorption observed in *n*-type direct gap quantum well infrared photodetectors (QWIPs) fabricated from the GaAs/AlGaAs and strained layer InGaAs/AlGaAs materials systems grown on GaAs substrates as well as developing multi-color QWIPs for 3-5  $\mu\text{m}$  MWIR and 8-14  $\mu\text{m}$  LWIR applications. In this research project, we have conducted theoretical and experimental studies on normal incidence absorption in *n*-type direct gap QWIPs formed on AlGaAs/GaAs and InGaAs/AlGaAs materials systems. A theoretical model for calculating the TE and TM transition ratios for the symmetrical LWIR- and step MWIR-QWIPs has been developed in this work. The role of strain on the normal incidence absorption has been investigated. We have also calculated the absorption coefficients for several *n*-type QWIPs, including both the high -strain MWIR QWIP and LWIR TC-QWIPs. Analysis of simplified QWIPs for low photon background applications has been made in this work. We have also studied the quantum confined Stark effect in a weakly coupled double quantum wells structure. Experimental studies on three QWIP samples with different device structures, processing parameters and experimental conditions have been made to investigate the various effects on the normal incidence absorption. Several new simplified QWIPs have been designed and processed which show strong evidence of normal incidence absorption. Finally, a novel four-stack, four-color QWIP has been designed, fabricated and characterized. Several journal and conference papers have been published and presented from this work.

## 1. Theoretical Study of Normal Incidence Absorption in $n$ -type Direct Gap QWIPs

### 1.1 Introduction

Ever since West and Eglash observed experimentally a large oscillator strength of the intersubband transition in a series of multiquantum wells [1] and Levine *et al.* demonstrated the first quantum well infrared photodetector (QWIP) using GaAs/Al<sub>x</sub>Ga<sub>1-x</sub>As multiquantum well structure [2], a considerable amount of works have been reported in this field [3,4,5]. Taking advantages of band gap engineering and the maturity of the III-V semiconductor materials growth and processing technology, large uniform GaAs/AlGaAs focal plane arrays (FPAs) with low noise equivalent temperature difference, high resolution, high production yield, high speed, low cost and low power consumption have been demonstrated in recent years.

In the development of QWIPs, an important issue is normal incidence absorption. It is well known that normal incidence absorption is forbidden in  $n$ -type direct gap QWIPs due to quantum mechanical selection rules. As a result, it is a common practice to use Brewster angle or the 45° bevel angle incidence configuration, or optical grating to couple the normal incidence light. These coupling schemes complicate the fabrication of focal plane arrays and also cause cross talk between the adjacent pixels. Due to this reason, there has been a continuous interest in the study of normal incidence absorption in QWIPs.  $P$ -type QWIPs with normal incidence absorption have been demonstrated [6,7,8] and the mechanism is due to the band mixing between the heavy- and light- hole states.

However, due to the large heavy effective mass and low mobility of holes, the responsivity of  $p$ -type QWIPs are substantially smaller than that of  $n$ -type QWIPs. Normal incidence absorption  $n$ -type QWIPs due to anisotropic effective-mass tensors grown other than (100) substrate have been suggested and demonstrated [9,10,11,12]. The development in this type of normal incidence absorption QWIPs is limited by the difficulties of materials growth and the tilted ellipsoidal band structure also causing some complication in design and controllability.

Normal incidence absorption in  $n$ -type direct gap QWIPs was first observed by Peng *et al.* [13] in InGaAs/InAlAs system. In addition, normal incidence absorption in other  $n$ -type direct gap QWIPs were also repeated [14-21], including  $\text{In}_x\text{Ga}_{1-x}\text{As}/\text{In}_y\text{Al}_{1-y}\text{As}$  [13,14,16,17],  $\text{In}_x\text{Ga}_{1-x}\text{As}/\text{GaAs}$  [15,18],  $\text{GaAs}/\text{Al}_x\text{Ga}_{1-x}\text{As}$  [19,20,21] and  $\text{In}_x\text{Ga}_{1-x}\text{As}/\text{GaAs}/\text{Al}_y\text{Ga}_{1-y}\text{As}$  [20,21]. Theoretically, several mechanisms have been proposed for the possibility of normal incidence absorption in  $n$ -type direct gap QWIPs. However, none of these theories is able to explain the experimentally observed value.

## 1.2 Summary of existing theories on normal incidence absorption mechanisms

In 1981 Zaluzny pointed out that in narrow gap semiconductors spin-orbit coupling can induce spin-flip excitations by IR radiation polarized parallel to the layer surfaces [22]. Shik considered the four-band Kane model and found that both spin-orbit coupling and the variation of electron effective masses in space can induce normal incidence absorption in  $n$ -type direct band gap quantum well structure [23,24]. Eight-band Kane model has been considered in the selection rules of intersubband transitions in the conduction band quantum wells by Yang *et al.* [25]. Yang investigated the effect of

the spatial variation of effective masses and proposed several structures to enhance the normal incidence absorption in  $n$ -type direct gap QWIPs [26, 27]. Peng *et al.* developed a generalized 14 - band model to discuss normal incidence absorption in  $n$ -type direct gap QWIPs [28]. They showed that by taking into account the coupling between  $\Gamma_1^c \rightarrow \Gamma_{15}^v$ ,  $\Gamma_1^c \rightarrow \Gamma_{15}^c$  and  $\Gamma_{15}^c \rightarrow \Gamma_{15}^v$  bands, a nearly equal TE and TM absorption can be obtained. However, this has been shown to be inaccurate lately [29], and it is revealed recently that multiband coupling effect is not sufficient to explain the observed normal incidence absorption [30]. The above cited studies will be briefly summarized as follows.

#### 1.2.1 One- band model considering spatial variation of effective mass

Within one-band model, if the effective masses of electrons in the quantum well and barrier layers are taken to be the same, the in-plane polarization absorption is prohibited. This is due to the fact that the oscillator strength of the in-plane (for example, the x-direction) polarization absorption is proportional to the overlap of the wave functions of initial and final states; since different states are orthogonal, the oscillator strength will be zero, i.e.,

$$f_x \sim \frac{1}{m^*} \langle \phi_f | \phi_i \rangle = 0 \quad (1)$$

where  $f_x$  is the x-polarization absorption oscillator strength,  $m^*$  is the effective mass of electron,  $\phi_i$  and  $\phi_f$  are the initial and final state wavefunctions, respectively. This is schematically shown in figure 1.2.1 (a).



By taking into account the spatial variation of the electron effective mass, the factor of the inverse mass cannot be taken out of the integral in equation (1), and hence  $f_x$  will have a nonzero value, *i.e.*,

$$f_x \sim \left\langle \phi_f \left| \frac{1}{m^*(z)} \right| \phi_i \right\rangle \neq 0 \quad (2)$$

This is schematically shown in figure 1.2.1(b). The above calculation shows that the oscillator strength of TE absorption is generally less than 1% of that of TM absorption [27].

### 1.2.2 Kane Model

Another way to study normal incidence absorption is to start from a four-band or an eight-band Kane model. Within Kane model, the band coupling and spin-orbit interaction cause the spin degenerate states to form two other degenerate states which include both the spin-up and spin-down states, as shown in figure 1.2.2. Normal incidence absorption can occur between states having the same dominant states and states having different dominant states. The oscillator strength ratio of the normal incidence absorption between the same spin group to the z-polarization absorption is almost the same as the ratio mentioned in section 1.2.1, which is less than 1%. The oscillator strength ratio  $R$  of the normal incidence absorption between different spin groups to the z-polarization absorption is proportional to [23]

$$R \approx \left| \frac{1}{3} \frac{\Delta}{E_g + \frac{2}{3}\Delta} \right|^2 \quad (3)$$

where  $E_g$  is the band gap, and  $\Delta$  is the spin-orbit splitting of the well material, respectively. For GaAs, with  $E_g \sim 1.5$  eV and  $\Delta \sim 0.34$  eV, we obtain  $R \sim 0.004$ . For InGaAs,  $E_g \sim 1$  eV,  $\Delta \sim 0.37$  eV and one finds  $R \sim 0.01$ . Thus, normal incidence absorption cannot be explained using the four- or eight- band Kane model.

### 1.2.3 Multi-band coupling effects

Peng *et al.* [28] pointed out the important influence of multi-band coupling effect on intersubband transitions. They claimed that coupling of higher conduction band  $\Gamma_{15}^c$  with the valence band  $\Gamma_{15}^v$  and lowest conduction band  $\Gamma_1^c$  can cause normal incidence absorption, as shown in figure 1.2.3, and they also claimed that normal incidence absorption can be as strong as the z-polarization absorption. However, their analysis turned out to be incorrect and a more elaborated numerical calculation showed that normal incidence absorption is usually negligible within this multiband scheme [30].

## **1.3 Theoretical Study of Normal Incidence Absorption in *n*-type QWIPs**

### 1.3.1 One- band model taking into account spatial variations of both the effective mass and refractive index

We have performed a theoretical study of normal incidence absorption on several *n* – type QWIP structures which showed obvious normal incidence absorption based on a one-band model taking into account spatial variations of both the effective mass and refractive index. The one- band model works well for the study of TM absorption. On the other hand, we think that if one-band model cannot explain normal incidence absorption, the multi-band model may not be able to explain the observed normal incidence

absorption in *n*-type QWIPs either. Since one-band model already includes the influences of valence bands and higher conduction bands through the effective mass of electrons.

The envelope function in the *z*- (the growth) direction  $\varphi(z)$  satisfies the following equation

$$\left\{ \frac{p^2}{2m^*(z)} + \left( p \frac{1}{2m^*(z)} \right) \cdot p + V(z) \right\} \varphi(z) = \varepsilon \varphi(z) \quad (4)$$

where  $p$  is the momentum operator of electron and  $m^*(z)$  is the space-variant electron effective mass,  $V(z)$  and  $\varepsilon$  are the potential and the energy of electron in the *z*- direction, respectively.

We consider the symmetric and step MQW structure with one bound state in the wells, as shown schematically in figure 1.3.1. The coordinates adopted in the calculation are shown in figure 1.3.2. The wave function of the bound state can be written as

$$\varphi_1 = \begin{cases} A_1 \exp(\kappa_1 z), & z < -L_w/2. \\ B_1 \cos(k_1 z), & |z| \leq L_w/2. \\ A_1 \exp(-\kappa_1 z), & z > L_w/2. \end{cases} \quad (5)$$

where  $L_w$  is the well width,  $\kappa_1 = (2m_b^* (V_b - E_1)/\hbar^2)^{1/2}$ ,  $k_1 = (2m_w^* E_1/\hbar^2)^{1/2}$ ,  $m_b^*$  and  $m_w^*$  are the electron effective masses in the barrier and well, respectively,  $V_b$  is the barrier height,  $E_1$  is the energy level of the bound state.

From the boundary condition one obtains

$$A_1 = B_1 \cos(k_1 L_w/2) \exp(\kappa_1 L_w/2) \quad (6)$$

The wave function for the continuum state with odd parity can be written as

$$\varphi_2 = \begin{cases} A_2 \sin(k_{2b} z - \delta_2), & z < -L_w/2. \\ B_2 \sin(k_{2w} z), & |z| \leq L_w/2. \\ A_2 \sin(k_{2b} z + \delta_2), & z > L_w/2. \end{cases} \quad (7)$$

The boundary conditions yield

$$B_2 = A_2 \left[ \sin^2 \left( \frac{k_{2w} L_w}{2} \right) + \left( \frac{m_b^* k_{2w}}{m_w^* k_{2b}} \right)^2 \cos^2 \left( \frac{k_{2w} L_w}{2} \right) \right]^{-\frac{1}{2}} \quad (8a)$$

and  $\delta_2$  can be determined as

$$\delta_2 = \arcsin \left[ \frac{B_2}{A_2} \sin \left( \frac{k_{2w} L_w}{2} \right) \right] - \frac{k_{2b} L_w}{2} \quad (8b)$$

Similarly, one can obtain the wave function of the first even parity continuum state as

$$\varphi_3 = \begin{cases} A_3 \cos(k_{3b} z - \delta_3), & z < -L_w/2. \\ B_3 \cos(k_{3w} z), & |z| \leq L_w/2. \\ A_3 \cos(k_{3b} z + \delta_3), & z > L_w/2. \end{cases} \quad (9)$$

where

$$B_3 = A_3 \left[ \cos^2 \left( \frac{k_{3w} L_w}{2} \right) + \left( \frac{m_b^* k_{3w}}{m_w^* k_{3b}} \right)^2 \sin^2 \left( \frac{k_{3w} L_w}{2} \right) \right]^{-\frac{1}{2}} \quad (10a)$$

and

$$\delta_3 = \arccos \left[ \frac{B_3}{A_3} \cos \left( \frac{k_{3w} L_w}{2} \right) \right] - \frac{k_{3b} L_w}{2} \quad (10b)$$

In Eqs. (7-10),  $k_{ib} = (2m_b^*(E_i - V_b)/\hbar^2)^{1/2}$ ,  $k_{iw} = (2m_w^*E_i/\hbar^2)^{1/2}$ . The energy level of the bound state and the central energy of the continuum states can be determined by the transfer matrix method. Since the barrier is much wider than the well, we can assume  $A_2 = A_3 \approx (2/L_w + L_b)^{-1/2}$

The photon-electron interaction Hamiltonian can be formulated as

$$H_{ph} = \frac{e}{4c} e^{iq \cdot r} A_0 \vec{e} \cdot \left( \frac{1}{m^*} p + p \frac{1}{m^*} \right) \quad (11)$$

where  $q$  is the wave vector of the optical field.  $A_0$  and  $\mathbf{e}$  are the amplitude and direction of the vector potential.

Incorporating the Hamiltonian in Eq.(11) into the transition matrix between the initial and final states, the oscillator strength due to in-plane polarization (chosen to be the  $x$  - direction) transition can be expressed as

$$f_{if}^x = \frac{2}{m_w^* \hbar \omega} \left| \left( 1 - \frac{m_w^*}{m_b^*} \sqrt{\frac{n_w}{n_b}} \right) \hbar k_x \langle \varphi_f | \varphi_i \rangle_w \right|^2 \quad (12)$$

and the oscillator strength due to the  $z$  - direction polarization transition is

$$f_{if}^z = \frac{2 \hbar^2}{m_w^* \hbar \omega} \left| \langle \varphi_f | \frac{\partial}{\partial z} | \varphi_i \rangle_w + \frac{m_w^*}{m_b^*} \sqrt{\frac{n_w}{n_b}} \langle \varphi_f | \frac{\partial}{\partial z} | \varphi_i \rangle_b + \frac{1}{2} \left( 1 - \frac{m_w^*}{m_b^*} \sqrt{\frac{n_w}{n_b}} \right) \left( \varphi_f^* \left( -\frac{L_w}{2} \right) \varphi_i \left( -\frac{L_w}{2} \right) - \varphi_f^* \left( \frac{L_w}{2} \right) \varphi_i \left( \frac{L_w}{2} \right) \right) \right|^2 \quad (13)$$

where  $n_w$  and  $n_b$  are the refractive index of the well and barrier, respectively.

It can be seen from Eq.(12) that in the case of symmetrical quantum well the in-plane transition oscillator strength will be zero. Denoting the ratio between the oscillator strength of  $x$  polarization  $1 \rightarrow 3$  transition and that of  $z$  polarization  $1 \rightarrow 2$  transition as  $R$ .

After some manipulations, we get

$$R = \frac{X^2(E_2 - E_1)}{Y^2(E_3 - E_1)} \quad (14)$$

where

$$X = k_z \left( 1 - \frac{m_w^*}{m_b^*} \sqrt{\frac{n_w}{n_b}} \right) \left[ \frac{\sin(k_{3w} + k_1)L_w/2}{k_{3w} + k_1} + \frac{\sin(k_{3w} - k_1)L_w/2}{k_{3w} - k_1} \right] \left[ \cos^2\left(\frac{k_{3w}L_w}{2}\right) + \left(\frac{m_b^*k_{3w}}{m_w^*k_{3b}}\right)^2 \sin^2\left(\frac{k_{3w}L_w}{2}\right) \right]^{-\frac{1}{2}} \quad (15a)$$

and

$$Y = k_1 \left[ \frac{\sin(k_{2w} - k_1)L_w/2}{k_{2w} - k_1} - \frac{\sin(k_{2w} + k_1)L_w/2}{k_{2w} + k_1} \right] \left[ \sin^2\left(\frac{k_{2w}L_w}{2}\right) + \left(\frac{m_b^*k_{2w}}{m_w^*k_{2b}}\right)^2 \cos^2\left(\frac{k_{2w}L_w}{2}\right) \right]^{-\frac{1}{2}} \\ + 2 \cos(k_1 L_w/2) K_1 \frac{m_w^*}{m_b^*} \sqrt{\frac{n_w}{n_b}} \frac{K_1 \sin\left(\frac{k_{2b}L_w}{2} + \delta_2\right) + k_{2b} \cos\left(\frac{k_{2b}L_w}{2} + \delta_2\right)}{K_1^2 + K_{2b}^2} + \left( 1 - \frac{m_w^*}{m_b^*} \sqrt{\frac{n_w}{n_b}} \right) \cos\left(\frac{k_1 L_w}{2}\right) \sin\left(\frac{k_{2b}L_w}{2} + \delta_2\right) \quad (15b).$$

The results for step MQW structure can be obtained in a similar way. The results are rather tedious and will not be listed here.

The systems under study are 24ÅIn<sub>0.35</sub>Ga<sub>0.65</sub>As/5Å GaAs/300ÅAl<sub>0.38</sub>Ga<sub>0.62</sub>As[21], 55ÅGaAs/500ÅAl<sub>0.27</sub>Ga<sub>0.73</sub>As[21], 44ÅIn<sub>0.34</sub>Ga<sub>0.66</sub>As/250ÅGaAs[15], 40ÅIn<sub>0.32</sub>Ga<sub>0.68</sub>As/500 ÅGaAs[34], 40Å In<sub>0.3</sub>Ga<sub>0.7</sub>As/300Å GaAs[31]. The temperature used in the calculation is 77 K and the parameters used in the calculation can be found from [32]. In the InGaAs/AlGaAs and InGaAs/GaAs system, lattice mismatch between these two systems will cause strain. Strain effects induced by lattice-mismatch will modify the energy band structure. For conduction band at  $k=0$ , strain will cause a rigid shift  $\Delta E_C$ . For valence band at  $k=0$ , strain has three effects on it: strain will introduce a rigid shift for all the three valence bands (heavy-hole, light-hole and split-off bands), this is caused by the hydrostatic component  $\Delta E_H$ , strain will also cause the reduction of symmetry and therefore cause the splitting of heavy-hole and light-hole bands, which is caused by the

shear uniaxial component  $\Delta E_U$ ; strain can also cause the coupling of the light-hole band and the split-off band.  $\Delta E_C$ ,  $\Delta E_H$  and  $\Delta E_U$  can be expressed, respectively as

$$\Delta E_C = 2a_c \frac{c_{11} - c_{12}}{c_{11}} \varepsilon_{||} \quad (16a)$$

$$\Delta E_H = 2a_v \frac{c_{11} - c_{12}}{c_{11}} \varepsilon_{||} \quad (16b)$$

$$\Delta E_U = -b_v \frac{c_{11} + 2c_{12}}{c_{11}} \varepsilon_{||} \quad (16c)$$

where  $a_c$  is the hydrostatic deformation potential of conduction band.  $a_v$  and  $b_v$  are the hydrostatic and uniaxial deformation potentials of valence bands, respectively.  $c_{ij}$ 's are the elastic constants, and  $\varepsilon_{||}$  is the in-plane strain component.

The energy band gaps under strain for the heavy hole, light hole and split-off bands at  $k=0$  are given respectively by

$$E_g^{C,HH} = E_g^0 + \Delta E_C + \Delta E_H + \Delta E_U \quad (17a)$$

$$E_g^{C,LH} = E_g^0 + \Delta E_C + \Delta E_H - \frac{1}{2} \left( \Delta E_U - \Delta_0 + \sqrt{\Delta_0^2 + 2\Delta_0 \Delta E_U + 9\Delta E_U^2} \right) \quad (17b)$$

$$E_g^{C,SO} = E_g^0 + \Delta E_C + \Delta E_H - \frac{1}{2} \left( \Delta E_U - \Delta_0 - \sqrt{\Delta_0^2 + 2\Delta_0 \Delta E_U + 9\Delta E_U^2} \right) \quad (17c)$$

where  $\Delta_0$  and  $E_g^0$  are the spin-orbit splitting and energy band gap without strain, respectively.

As mentioned before, strain can cause the reduction of symmetry. As a result, the effective mass of the electron in the conduction band will become anisotropic (i.e., the effective mass along the growth direction will be different from the in-plane one). Under

strain, the in- plane effective mass  $m_c^{\parallel}$  and the growth direction effective mass  $m_c^z$  can be expressed as [33]

$$\frac{m_0}{m_c^{\parallel}} = 1 + \frac{E_p}{6} \left[ \frac{3}{E_g^{C.MH}} + \frac{(\alpha - \sqrt{2}\beta)^2}{E_g^{C.LH}} + \frac{(\beta + \sqrt{2}\alpha)^2}{E_g^{C.SO}} \right] \quad (18a)$$

$$\frac{m_0}{m_c^z} = 1 + \frac{E_p}{3} \left[ \frac{(\sqrt{2}\alpha - \beta)^2}{E_g^{C.LH}} + \frac{(\sqrt{2}\beta + \alpha)^2}{E_g^{C.SO}} \right] \quad (18b)$$

where  $m_0$  is the free electron mass,  $E_p$  is the energy related to the momentum matrix element of transition from the valence band to the lowest conduction band.  $\alpha$  and  $\beta$  are quantities introduced by the strain. The variation of electron effective mass of InGaAs on (001) GaAs with In composition is shown in figure 1.3.3. In our calculation we have taken into account this effect. We calculated the value of  $R$  at  $k_F = (2m_{\parallel}^* E_F / \hbar^2)^{1/2}$  and the results are listed in Table 1.1.

System	R
24Å In <sub>0.35</sub> Ga <sub>0.65</sub> As/5Å GaAs/300Å Al <sub>0.38</sub> Ga <sub>0.62</sub> As	$7.1 \times 10^{-3}$
55Å GaAs/500Å Al <sub>0.27</sub> Ga <sub>0.73</sub> As	$3.5 \times 10^{-4}$
44Å In <sub>0.34</sub> Ga <sub>0.66</sub> As/250Å GaAs	$1.1 \times 10^{-4}$
40Å In <sub>0.32</sub> Ga <sub>0.68</sub> As/500Å GaAs	$0.79 \times 10^{-4}$
40Å In <sub>0.3</sub> Ga <sub>0.7</sub> As/300Å GaAs	$0.92 \times 10^{-4}$

Table 1.1 Calculated results of  $R_1$  and  $R_2$  for the MWIR and LWIR QWIPs at  $k_F = (2m_{\parallel}^* E_F / \hbar^2)^{1/2}$ .



It is noted from this table that the experimentally observed normal incidence absorption cannot be explained by the model depicted above.

### 1.3.2 The role of strain on normal incidence absorption

Several  $n$ -type QWIP structures showing strong normal incidence absorption are based on strained-layer InGaAs/AlGaAs systems which have lattice mismatch between the InGaAs quantum well and GaAs substrate and hence cause significant strain. We have studied the high-strain InGaAs/AlGaAs QWIP to see if the compressive strain is uniquely responsible for the observed normal incidence absorption.

The electron-photon interaction Hamiltonian can be written as

$$H' = \frac{e}{2c} \vec{A} \cdot \vec{W} \cdot \vec{p} \quad (19)$$

where  $e$  is the electronic charge,  $c$  is the velocity of light,  $\vec{A}$  is the vector potential,  $\vec{W}$  is the inverse mass tensor and  $\vec{p}$  is the momentum operator.

Considering the transition between the two states, with the wave functions for the initial state denoted as  $\psi_i$  and the final state denoted as  $\psi_f$ , i.e.,

$$\Psi_i = e^{ik_i \rho} F_i(z) u_i(r) \quad (20a)$$

$$\Psi_f = e^{ik_f \rho} F_f(z) u_f(r) \quad (20b)$$

It can be shown that the transition matrix element between the initial state  $i$  and final state  $f$ ,  $M_{fi}$  is proportional to

$$M_{fi} \sim A_x W_{xx} p_x + A_y W_{yy} p_y + A_z A_z p_z \quad (21)$$

In the case of biaxial strain, the inverse mass tensor becomes

$$\vec{W} = \begin{pmatrix} \frac{1}{m_c^x} & & \\ & \frac{1}{m_c^y} & \\ & & \frac{1}{m_c^z} \end{pmatrix} \quad (22)$$

For the TE polarization, for example, taking  $A$  in the  $x$ -direction, since  $W_{xz}=0$ ,  $M_{fi}$  will be zero. This is due to the fact that in InGaAs/GaAs system the strain direction coincides with the main axes of energy ellipsoid, no non-diagonal component of inverse mass tensor will occur. It is shown here that the strain can not be solely responsible for the observed normal incidence absorption.

#### **1.4 Other possible normal incidence absorption mechanisms**

##### **1.4.1 Interface roughness**

If the interface between the well and barrier is very rough, a normal incident light can be scattered into all directions and cause the absorption of normal incident light. However, modern MBE technology can grow very smooth interface in the III-V material systems such as GaAs/AlGaAs and InGaAs/AlGaAs. Even in the strained QWIPs, since the thickness of the well is within the critical thickness and the dislocation is localized and hence the interface is expected to be very good. Fluctuations of the order of one monolayer always are possible, but it is unlikely that this kind of fluctuations can cause normal incidence absorption. Since the refractive indexes and effective masses of two adjacent layers are usually quite similar.

##### **1.4.2 The effect of donor states**

Recently Ryzhii *et al.* proposed that doping might be responsible for normal incidence absorption [34]. They attributed the TM absorption to the transition from quantum well ground state to continuum state and TE absorption to the transition from the donor state to quantum well ground state (total energy exceeds the barrier height due to the in-plane energy component). However, it appears that their model cannot explain the coincidence of the transition peaks of TE and TM absorption. Their model shows that normal incidence does not depend on the doping concentration, which is in contrast with the experimental results observed by Wang *et al.* [31,35].

### 1.5 Conclusions

We have discussed theoretically the possible effects that might be responsible for the normal incidence absorption, including spatial variation of the effective mass, the role of high order bands, strain effect *etc.* None of these effects is able to cause normal incidence absorption which is comparable to the TM absorption. Our calculation on the QWIPs, which exhibit experimentally large normal incidence absorption, shows that the TE (normal incidence) absorption is about 1% of the TM absorption. No intrinsic physical reason is responsible for the observed normal incidence absorption. Therefore, the observed normal incidence absorption must be due to some unknown experimental conditions.

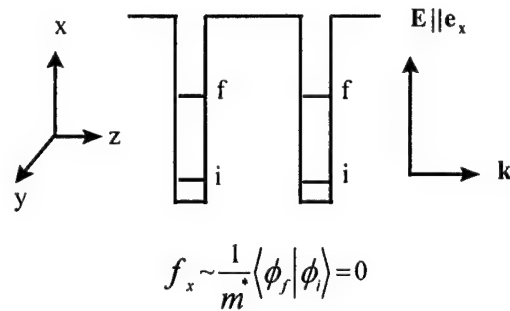


Figure 1.2.1(a). Under one- band constant electron effective mass approximation, in-plane polarization (normal incidence) absorption is prohibited.

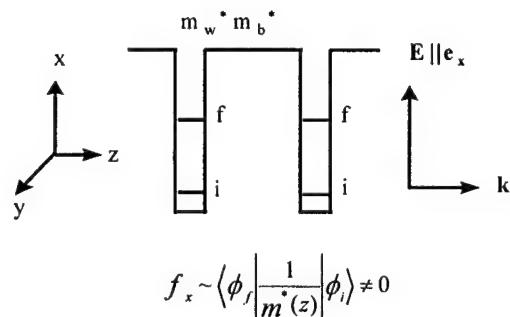


Figure 1.2.1(b) Under one- band space-variant electron effective mass approximation, in-plane polarization (normal incidence) absorption is allowed.

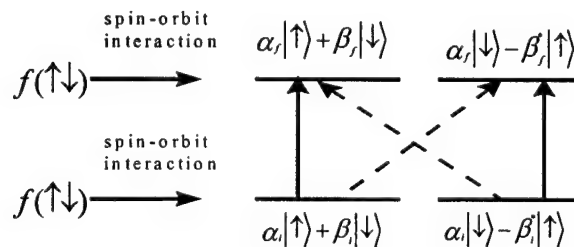


Figure 1.2.2 In Kane model, band coupling and spin-orbit interaction cause the spin degenerate states to form two new degenerate states which include both the spin- up and spin- down states. Normal incidence absorption can occur between states having same dominant spins (solid lines) and states having different dominant spins (dashed lines).

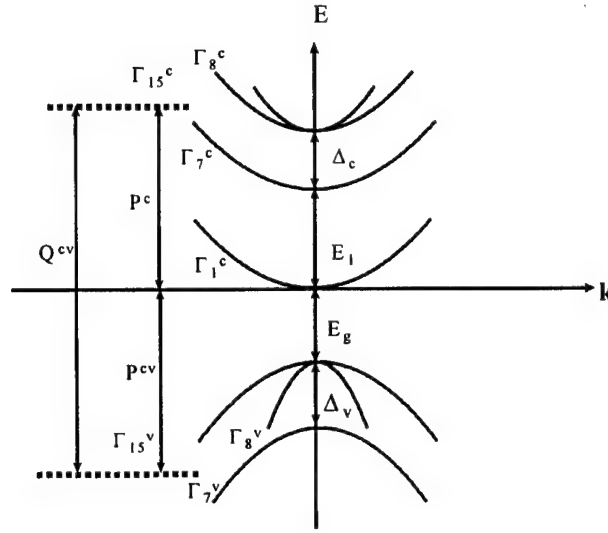


Figure 1.2.3 Coupling of the higher conduction band  $\Gamma_{15}^c$  with the valence band  $\Gamma_{15}^v$  (the coupling matrix is indicated by  $Q^{cv}$ ) and the lowest conduction band  $\Gamma_1^c$  (the coupling matrix is indicated by  $P^c$ ) can cause normal incidence absorption.

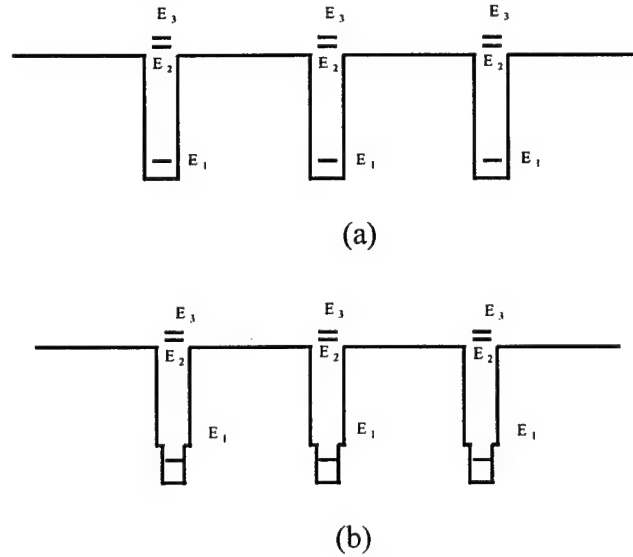
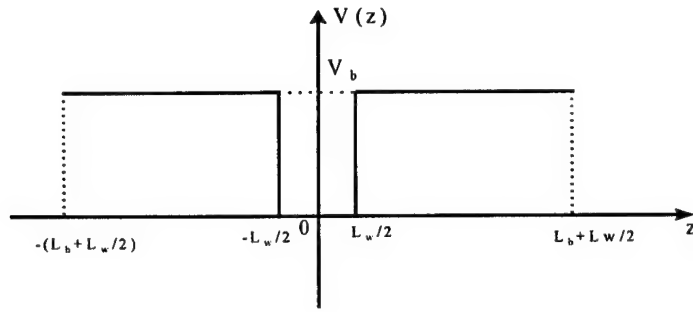
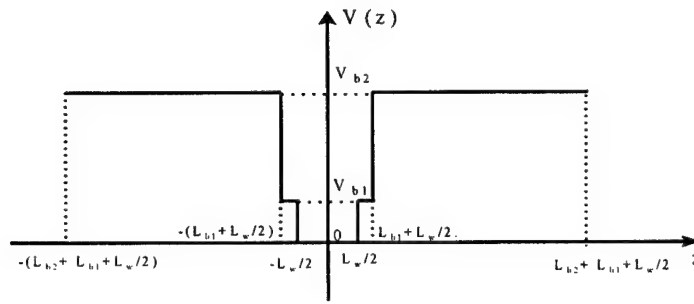


Figure 1.3.1 Schematic conduction band diagram of the symmetric and step MQW structure under consideration.  $E_1$  is the energy level of the bound state,  $E_2$  and  $E_3$  are the center energy levels of the first and second continuum states, respectively.



1.3.2 (a)



(b)

Figure 1.3.2 Coordinates adopted in the calculation for symmetric (a) and step (b) MQW structure. In (a),  $L_w$  is the well width,  $L_b$  is the barrier width and  $V_b$  is the barrier height. In (b),  $L_w$  is the well width,  $L_{b1}$  and  $L_{b2}$  are the first and second barrier widths, respectively,  $V_{b1}$  and  $V_{b2}$  are the first and second barrier heights, respectively.

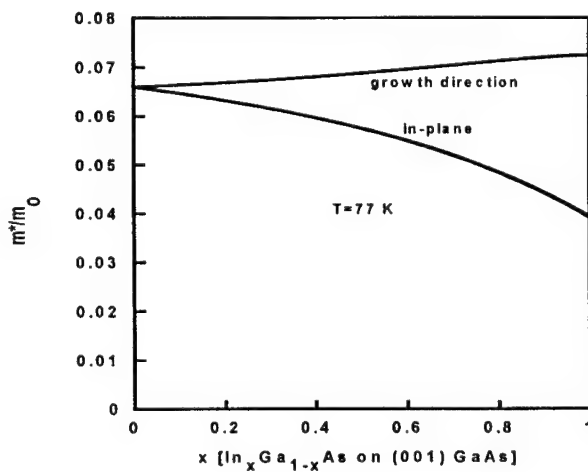


Figure 1.3.3 Variation of the effective mass of  $\text{In}_x\text{Ga}_{1-x}\text{As}$  on (001) GaAs.

## 2. Intersubband Absorption Coefficient in QWIPs

The responsivity of a QWIP can be written as

$$R_r = \frac{e}{h\nu} \eta_a p_e g \quad (23)$$

where  $h\nu$  is the incident photon energy,  $\eta_a$  is the quantum efficiency,  $p_e$  is the escape probability, and  $g$  is the optical gain. The quantum efficiency  $\eta_a$  is given by

$$\eta_a = \frac{1}{2} (1 - e^{-2\alpha l}) \quad (24)$$

where  $l$  is the length of the high-field domain, and  $\alpha$  is the absorption coefficient. It is seen from Eqs. (23) and (24) that absorption coefficient plays an important role in determining the responsivity of QWIPs. We have performed the calculation of absorption coefficients for several QWIP structures.

Considering an optical transition from the initial state 1 to the final state 2, the absorption coefficient can be written as

$$\alpha(\omega) = \frac{4\pi^2 e^2}{nc\omega} \int_{BZ} \frac{2d^3k}{8\pi^3} P_{12}^2 [f(E_1) - f(E_2)] \frac{\Gamma_{12}}{\pi} \frac{1}{(E_2 - E_1 - \hbar\omega)^2 + \Gamma_{12}^2} \quad (25)$$

where  $n$  is the refractive index,  $\omega$  is the incident light frequency,  $E_1$  and  $E_2$  are the energies of the initial and final states, respectively.  $f(E)$  is the Fermi-Dirac distribution functions.  $\Gamma_{12}$  is a broadening parameter. The momentum matrix element  $P_{12}$  is given by

$$P_{12} = -\frac{i\hbar}{m_c} \left\langle \phi_2 \left| \frac{\partial}{\partial z} \right| \phi_1 \right\rangle \quad (26)$$

$\phi_1$  and  $\phi_2$  are the growth direction envelope functions for the initial and final states, respectively.

We have used the above formula to calculate the absorption coefficient of some QWIPs, including two-stack, two-color MWIR QWIP [21] and TC QWIPs ( TC 206 and TC 301). In the calculation the broadening parameter was taken as 2 meV. The parameters used for calculating the absorption coefficient of two-stack , two-color MWIR QWIP is listed in Table 2.1. The parameters used for TC 206 and TC 310 are listed in Table 2.2(a) and Table 2.2(b), respectively.

Table 2.1. Parameters used in the absorption coefficient calculation of a two-stack, two-color MWIR QWIP at 300 K.

	GaAs	$\text{Al}_{0.38}\text{Ga}_{0.62}\text{As}$	$\text{In}_{0.35}\text{Ga}_{0.65}\text{As}$
$m_c^z (m_0)$	0.063	0.0961	0.0647
$m_c^{\parallel} (m_0)$	0.063	0.0961	0.0578
Eg (eV)	1.424	1.8979	1.0629
n	3.2989	3.1308	3.3693

Table 2.2(a) Parameters used in the absorption coefficient calculation of TC 206 at 77 K.

	$\text{Al}_{0.11}\text{Ga}_{0.79}\text{As}$	$\text{In}_{0.25}\text{Ga}_{0.75}\text{As}$	$\text{In}_{0.12}\text{Ga}_{0.88}\text{As}$
$m_c^z (m_0)$	0.0752	0.0667	0.0663
$m_c^{\parallel} (m_0)$	0.0752	0.0622	0.0643
Eg (eV)	1.6327	1.238	1.3717
n	3.221	3.3245	3.2941

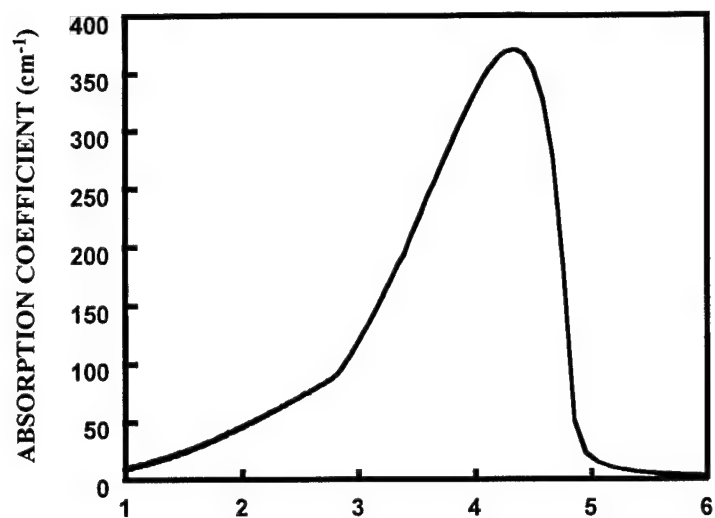


Table 2.2(b) Parameters used in the absorption coefficient calculation of TC 301.  
The temperature was taken as 77 K.

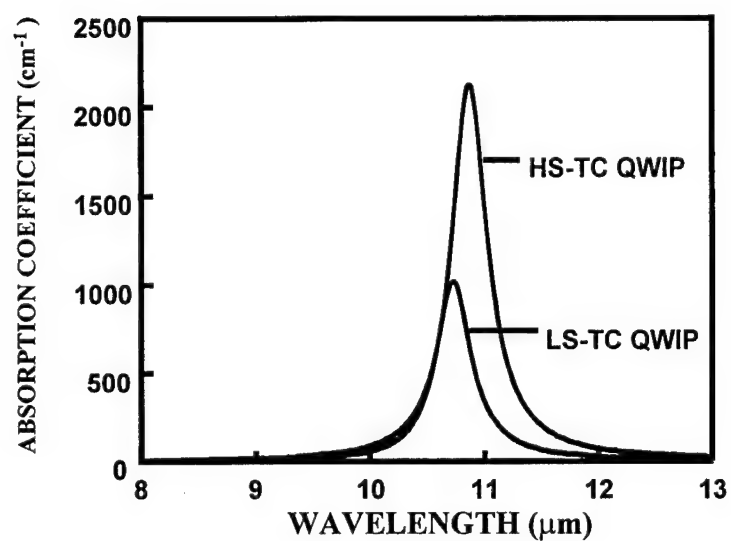
	GaAs	Al <sub>0.21</sub> Ga <sub>0.79</sub> As	In <sub>0.05</sub> Ga <sub>0.95</sub> As
$m_c^z (m_0)$	0.066	0.0836	0.066
$m_c^{\parallel} (m_0)$	0.066	0.0836	0.0652
Eg (eV)	1.508	1.7574	1.443
n	3.266	3.18	3.278

The calculated results are shown in figure 2.1. It is seen from figure 2.1 that the high-strain QWIP has higher absorption coefficient compared to that of low-strain QWIP. This is due to several reasons: (1) the high-strain QWIP has a deeper well and hence a large overlap of wave functions between the ground and the excited states; (2) the doping density in high-strain TC QWIP is higher and hence the Fermi energy is higher, which can increase the term of  $f(E_1)-f(E_2)$  in Eq. (25) and therefore increase the absorption coefficient correspondingly.

The calculation of absorption coefficient shown here provides a good basis for further study of the relationship among responsivity, optical gain, and optical absorption coefficient.



(a) HS-QWIP (MWIR)



(b) LS and HS-TC QWIP(LWIR).

Figure 2.1 Absorption coefficient of (a) high strain MWIR QWIP and

(b) TC QWIPs.

### 3. Study of Normal Incidence Absorption in N-type QWIPs

#### 3.1 Influence of experimental conditions on normal incidence absorption

In this section, we describe the experimental study of the normal incidence absorption in *n*-type direct gap QWIPs. All three QWIP samples discussed here were grown on semi-insulating GaAs substrate (100) by molecular beam epitaxy (MBE) technique. Sample-1 [20] was designed to have two stacks of quantum wells as the active region with a contact layer in between the two stacks. The bottom MWIR stack has 20 periods of 30 nm  $\text{Al}_{0.38}\text{Ga}_{0.62}\text{As}$  barrier and 2.4 nm  $\text{In}_{0.35}\text{Ga}_{0.65}\text{As}$  sandwiched between two 0.5 nm GaAs. The top LWIR stack consists of 20 periods of 50 nm  $\text{Al}_{0.27}\text{Ga}_{0.73}\text{As}$  barrier and 5.5 nm GaAs well. The Si doping density in the wells is  $2.5 \times 10^{18} \text{cm}^{-3}$  for the first stack and  $0.7 \times 10^{18} \text{cm}^{-3}$  for the second stack. Sample-2 has similar structure parameters except that there is only three periods in each stack and no contact layer in between the two stacks. Sample-3 consists of only three quantum wells with three different barrier heights corresponding to three different peak wavelengths [36]. The detector consists of three 5.0 nm doped GaAs wells and four undoped AlGaAs barriers. There is no InGaAs involved and hence is free from strain caused by the lattice mismatch. The energy band diagrams for these three structures are shown in figure 3.1.1. The samples are processed using standard wet chemical etching, which produces certain edge area on the mesa. The area of the edge increases with the etching depth of the mesa, which depends on the QWIP structure thickness. Sample-1 was processed in two different ways in which the first method was a three-step photolithography. The top stack was etched down to the middle contact which gives the mesa for the LWIR stack defined by

the first photolithography. The MWIR stack is defined by etching the bottom stack to the bottom contact. The third lithography defines the metalization area, which covers the whole mesa area in this processing. The second method of processing was to etch the first stack down to the middle contact for the LWIR stack, while the MWIR mesa was formed by first totally removing the LWIR stack and then etching down to the bottom contact. The metal contact only occupies a small portion of the mesa area, and front illumination is used for the photoresponse measurements. Sample-2 used the second method in processing. Sample-3 has single color (LWIR), the metalization used the first processing geometry. The mesa areas are  $210 \times 210 \mu\text{m}^2$  for sample-1 and -2 using second processing method, and  $220 \times 360 \mu\text{m}^2$  for sample -3. The ratios of the edge area to the mesa area are 6.74%, 3.51% and 0.79%, respectively, for sample -1, -2, and -3.

The photocurrent spectra of the test devices were measured using a monochromator and a calibrated blackbody source. Figure 3.1.2 shows the responsivity of sample-1 as a function of bias voltage under normal incidence without grating, along with under  $45^\circ$  facet incidence. The peak wavelength of the MWIR stack under normal incidence is at  $4.4 \mu\text{m}$  with a maximum responsivity of  $0.2 \text{ A/W}$  at  $3.2 \text{ V}$ . It can be seen from this figure that the responsivity ratio of the normal incidence to the  $45^\circ$  facet incidence is about 41% at  $2 \text{ V}$ . For the LWIR stack, the peak wavelength of the normal incidence is at  $9.2 \mu\text{m}$  with a maximum responsivity of  $0.2 \text{ A/W}$  at  $2 \text{ V}$ . The responsivity ratio of the normal incidence to the  $45^\circ$  facet incidence is about 40% at this bias. The data shown at  $2 \text{ V}$  used samples with second processing method. Using first processing method gave similar results. Figure 3.1.3 shows the responsivity of sample-2 as a

function of bias voltage under normal incidence without grating and the  $45^\circ$  coupling. The peak wavelength of the MWIR stack is at  $4.3\ \mu\text{m}$  with a maximum responsivity of  $0.17\ \text{A/W}$  at  $2.2\ \text{V}$ , while the peak wavelength of the LWIR stack is at  $8.4\ \mu\text{m}$  with a maximum responsivity of  $0.1\ \text{A/W}$  at  $-3\text{V}$ . The responsivity ratios of the normal incidence to the  $45^\circ$  incidence are 25% at  $2.5\ \text{V}$  and 46% at  $2\ \text{V}$ , for the LWIR and MWIR stack, respectively. Figure 3.1.4 shows the responsivity spectra of sample-3 for the normal incidence without grating under different biases. The responsivity is  $0.49\ \text{A/W}$  at the peak wavelength of  $7.5\ \mu\text{m}$  and bias voltage of  $-0.58\text{V}$ . Samples-2 and -3 have much smaller edge areas compared with sample-1 due to their much thinner active layer thickness, but they still exhibited a large normal incidence responsivity.

The three samples given above have very different mesa heights, which are  $3358\ \text{nm}$ ,  $1747\ \text{nm}$  and  $505\ \text{nm}$  for sample-1, -2 and -3, respectively. Since the top contact layer also contributes to the edge effect, sample-3 has not only a very thin active layer, but also a  $100\ \text{nm}$  top contact layer which gives a much thinner mesa height than the other two samples. The responsivity value of sample-3 in Fig. 3.1.4 demonstrates that a sample with a very small edge area can still have very large normal incident responsivity. Another concern is the edge of the substrate, which can also contribute, to the edge effect. Special attention has been given to eliminate the effect of the substrate edge by using a very small size beam as shown in Fig. 3.1.5. Normal incidence responsivity was observed in sample-3 using an IR beam spot size of  $317\ \mu\text{m}$  diameter. Standard setup for the photocurrent measurements has a blackbody beam size of around one inch diameter.

The roughness of the metal-semiconductor interface at the metal contact due to the metal alloying inter-diffusion is another possibility that causes photon diffraction to the in-plane direction. Two metal contact geometries used to process sample-1 and -2 give two quite different metal contact areas. The high responsivity of both sample -1 and -2 reveals that metal-semiconductor interface diffusion is not the dominant factor for normal incidence intersubband transitions.

Sample-1 and -2 have high concentration of indium in the InGaAs/AlGaAs which causes high strain when grown on GaAs substrate due to the lattice mismatch. The material of sample-3 uses only GaAs/AlGaAs with no InGaAs involved. The high responsivity observed in sample-3 at normal incidence demonstrates that the unstrained quantum wells can have high normal incidence absorption as well when short-periods quantum well is used.

### **3.2 Investigation of new S-QWIP structures**

We designed and processed several simplified (S-) QWIP structures for LWIR (QWIP-A) and MWIR (QWIP-B and -C) detection. We expect these QWIPs to show large responsivities due to the short period and hence a relatively large photoconductive gain. For the MWIR QWIPs, a very high indium composition of 37% is used in the InGaAs quantum well. The MWIR QWIP-C is almost the same as the MWIR QWIP-B except that a very small amount of phosphorous was added in the AlGaAs barrier layer. The phosphorus is expected to improve the interface property and thus enhances the overall performance of the device.

### 3.2.1 LWIR QWIP –A

The growth structure of LWIR QWIP-A is shown in figure 3.2.1. The dark current density of this device is shown in figure 3.2.2. The responsivity of this device under normal incidence at 35 K is shown in figure 3.2.3. The responsivity of this device under normal incidence at 77 K is shown in figure 3.2.4. Figure 3.2.5 shows the responsivity of this device under 45° incidence at 35 K and figure 3.2.6 shows the responsivity of this device under 45° incidence at 77 K. We have calculated the detectivity ( $D^*$ ) value of this device under normal incidence at 77 K. The results are listed in Table 3.2.1.

Table 3.2.1 Detectivity of LWIR QWIP-A under normal incidence at 77 K.

bias (V)	-1.5	-1.0	-0.5	0.5	1.0	1.5
$D^*(10^9 \text{cmHz}^{1/2}/\text{W})$	4.17	3.81	1.13	7.33	3.77	4.31

### 3.2.2 MWIR QWIP- B and C

We have also performed dark I-V and photoresponse measurements on two MWIR QWIPs, i.e., QWIP-B and QWIP-C. The layer structure of MWIR QWIP-B is shown in figure 3.2.7. The layer structure of QWIP-C is similar to that of QWIP-B, except the barrier thickness is 300 Å and as mentioned before, there is a very small amount of phosphorus added to the barrier layer. The dark current density of QWIP 467 and QWIP 475 are shown in figure 3.2.8 and figure 3.2.9, respectively. For QWIP-B, no photoresponse was observed, and the room temperature resistance of this QWIP device is

always very high ( $\geq 10\text{K } \Omega$ ). For QWIP-C, we were able to measure responsivity, and the result is shown in figure 3.2.10. The peak wavelength for this device is at  $3.9 \mu\text{m}$ . We have calculated the detectivity of this device under normal incidence at 77 K, and the results are listed in Table 3.2.2.

Table 3.2.2 detectivity of QWIP LWIR-C under normal incidence at 77 K.

bias (V)	-2	-1.5	-1	-0.5	0.5
$D^*$ ( $10^8 \text{cmHz}^{1/2}/\text{W}$ )	0.674	1.11	1.55	1.28	0.01

### 3.3 Normal incidence absorption in regular QWIPs and EQWIP

To explore the effect of substrate thinning on the normal incidence absorption, we have performed a comparison study on the following QWIP structures:



Table 3.3.1 The layer structures for the QWIP under compared study.

Layer	Thickness (Å)	Doping (cm <sup>-3</sup> )
GaAs	4000	3x10 <sup>18</sup>
Al <sub>0.27</sub> Ga <sub>0.73</sub> As	500	-
GaAs	55	5x10 <sup>17</sup>
Al <sub>0.27</sub> Ga <sub>0.73</sub> As	500	-
GaAs	10000	3x10 <sup>18</sup>
Al <sub>0.60</sub> Ga <sub>0.40</sub> As	1000	-
GaAs Substrate	-	-

The measurement of the QWIP device without removing the substrate was done at University of Florida (UF) and the measurement with substrate being removed was done at Lockheed Martin Vought Systems (LMVS). The dark current density of this device measured at UF is shown in figure 3.3.1. A comparison of the dark current density measured at UF and LMVS is shown in table 3.3.2

Table 3.3.2 Comparison of the dark current density of QWIP- D at 77K.

Bias (V)	Dark current density J (A/cm <sup>2</sup> )		J <sub>UF</sub> /J <sub>LM</sub>
	device V3 of LMVS	device processed at UF	
-0.25	6.78×10 <sup>-5</sup>	1.06×10 <sup>-4</sup>	1.56
-0.5	4.9×10 <sup>-4</sup>	8.05×10 <sup>-4</sup>	1.64
-1.0	1.9×10 <sup>-3</sup>	4.3×10 <sup>-3</sup>	2.26

The peak responsivity of QWIP-D with substrate was measured at both the normal incidence and 45° incidence illumination, and the results are shown in figure 3.3.2(a) and figure 3.3.2(b), respectively. It is seen from figure 3.3.2 that this device shows a rather strong normal incidence absorption. Table 3.3.3 lists the peak responsivity of this device under normal incidence and 45° incidence.

Table 3.3.3 Peak responsivity of QWIP-D under normal incidence and 45° incidence and their ratios at different biases.

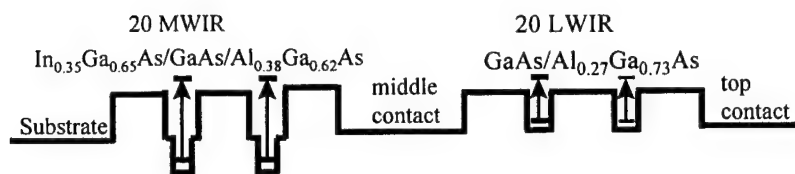
Bias (V)	normal incidence		45° incidence		$R_p(90^\circ)/R_p(45^\circ)$
	$\lambda_p(\mu\text{m})$	$R_p(\text{A/W})$	$\lambda_p(\mu\text{m})$	$R_p(\text{A/W})$	
-0.25	8.6	0.039	8.6	0.095	0.4105
-0.5	8.6	0.209	8.6	0.512	0.4082
-1.0	8.6	0.424	8.6	1.05	0.4038

The responsivity of this device with substrate being removed was also measured at LMVS, and no normal incidence absorption was found under this condition.

### 3.4 Conclusions

We have studied the effect of experimental conditions on normal incidence absorption in an *n*-type direct gap QWIP, including mesa form, mesa height, roughness of the metal-semiconductor interface, strain effect, substrate effect etc. From our study, we have found that the mesa form and height, metal-semiconductor interface and strain effects are not the key factors which cause normal incidence absorption in this QWIP.

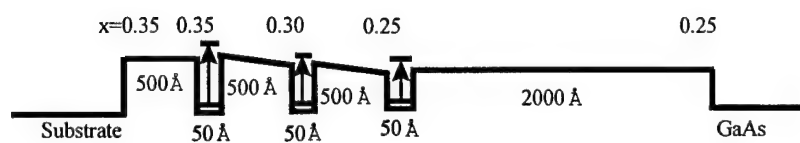
The samples used in our study are all grown on the semi-insulating GaAs substrate which does not absorb IR light, but scattering IR light diffracted back into the active quantum well layers can cause the observed normal incidence absorption. The presence of substrate could be the key factor responsible for the occurrence of normal incidence absorption in the n-type direct gap QWIPs.



(a)



(b)



(c)

Figure 3.1.1 Schematic energy band diagrams for QWIP samples -1 (a), -2 (b) and -3(c).

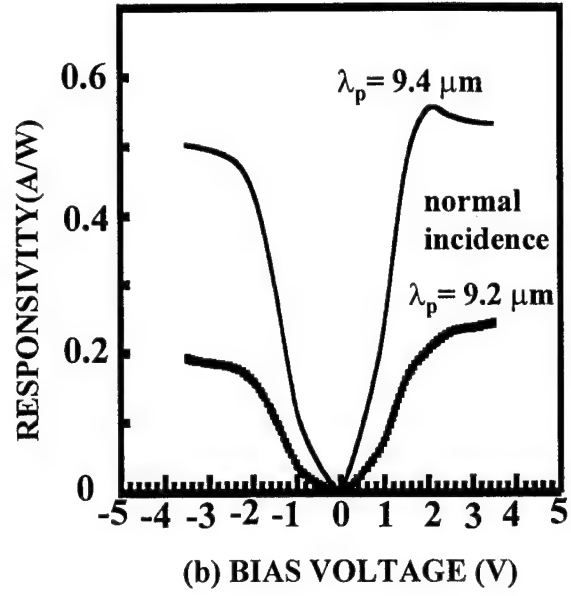
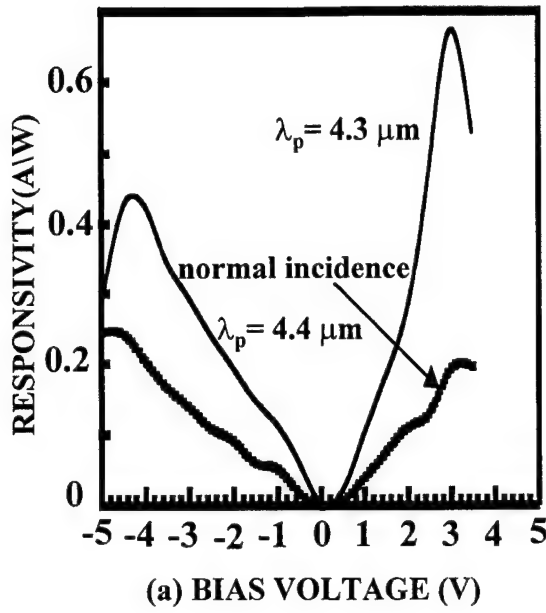


Figure 3.1.2 Responsivity of sample-1 (a) MWIR QWIP and (b) LWIR QWIP.

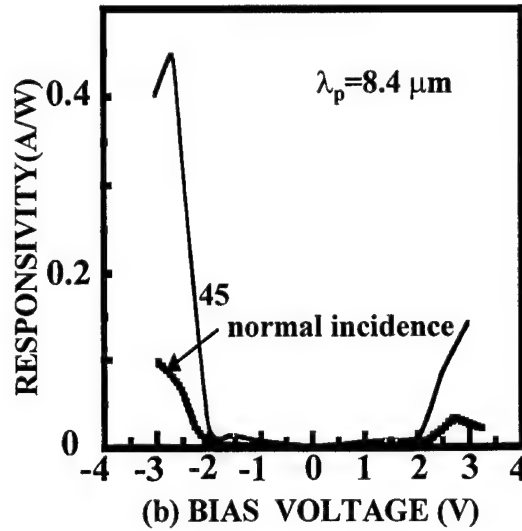
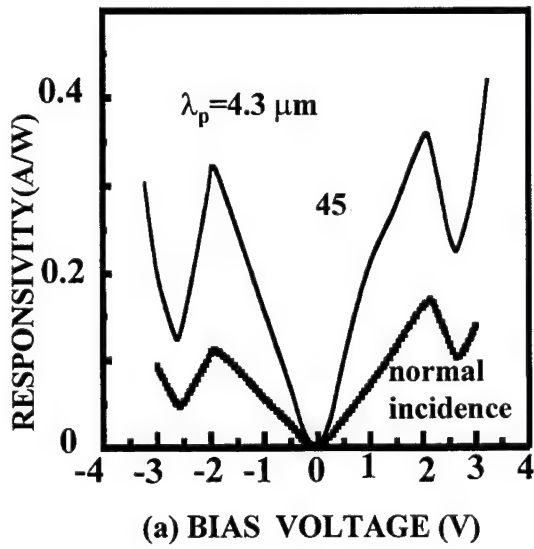


Figure 3.1.3 Responsivity of sample-2 (a) MWIR QWIP and (b) LWIR QWIP.

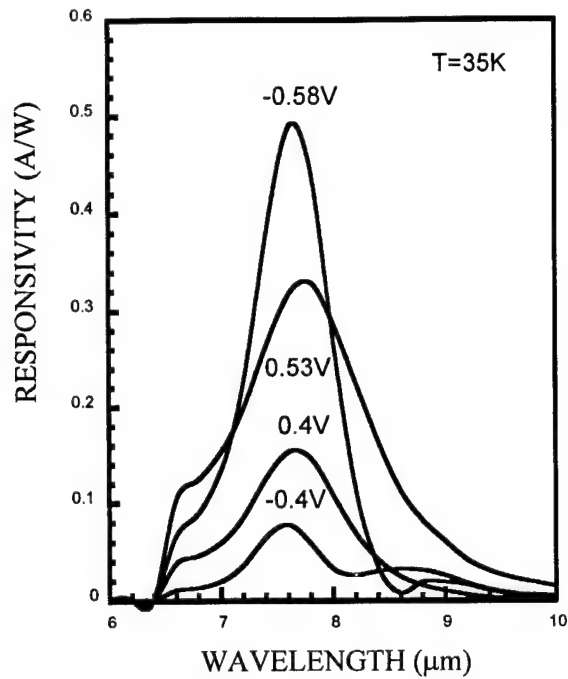


Figure 3.1.4 Responsivity of sample-3.

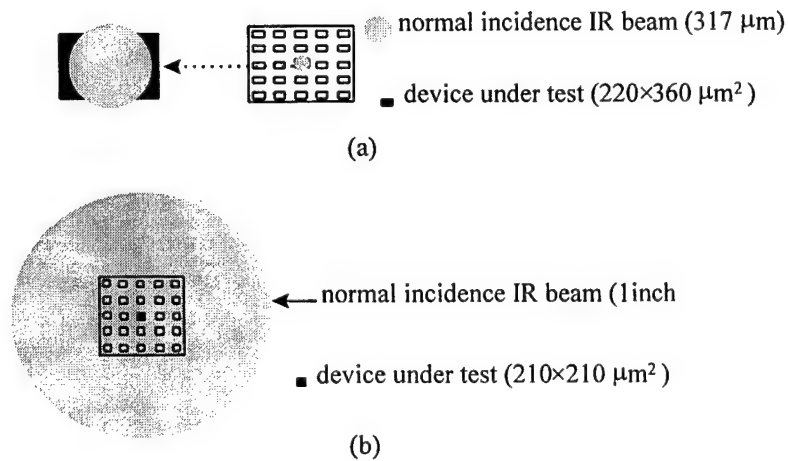


Figure 3.1.5 Schematic diagrams showing normal incidence illumination for (a) sample-3, using backside illumination with a beam size of 317  $\mu\text{m}$  diameter and (b) samples -1 and -2, using frontside illumination with a beam size of 1 inch diameter.

GaAs buffer layer, 4000 Å, $2 \times 10^{18} \text{ cm}^{-3}$	
Al <sub>0.29</sub> Ga <sub>0.71</sub> As, 500	
GaAs, 52 Å, $5 \times 10^{17} \text{ cm}^{-3}$	x5
Al <sub>0.29</sub> Ga <sub>0.71</sub> As, 500 Å, undoped	
GaAs buffer layer, 10000 Å, $3 \times 10^{18} \text{ cm}^{-3}$	
Al <sub>0.6</sub> Ga <sub>0.4</sub> As, 1000 Å, undoped	
GaAs S.I. substrate	

Figure 3.2.1 Layer structure of LWIR QWIP-A.

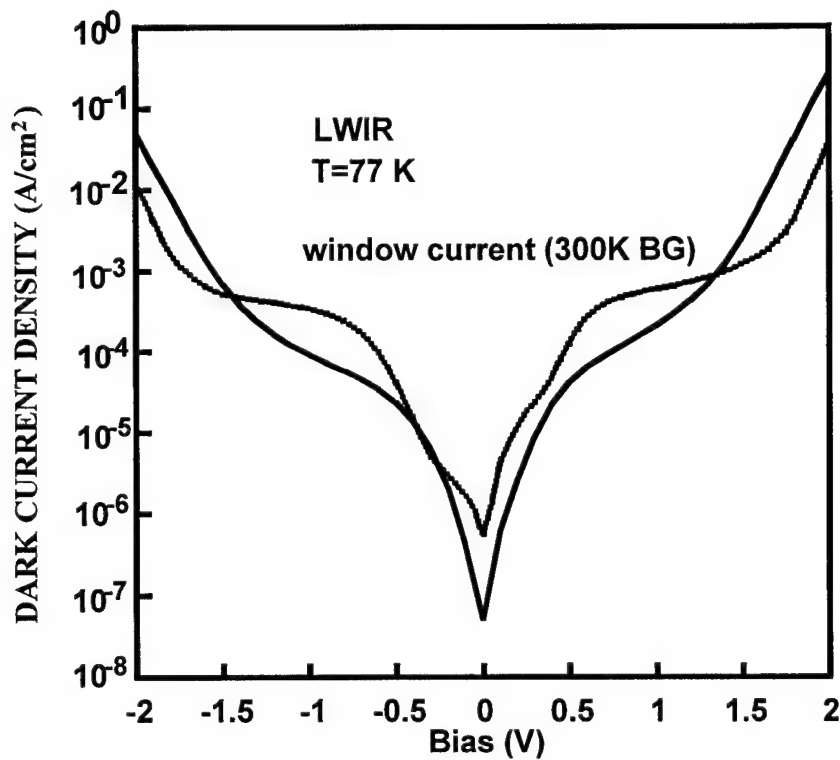


Figure 3.2.2 Dark current density of LWIR QWIP-A at 77 K.

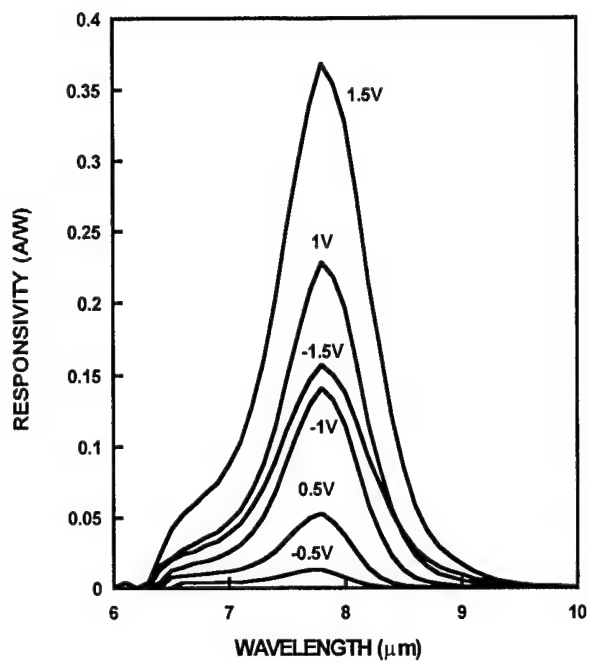


Figure 3.2.3 Responsivity of LWIR QWIP-A under normal incident illumination at 35 K.

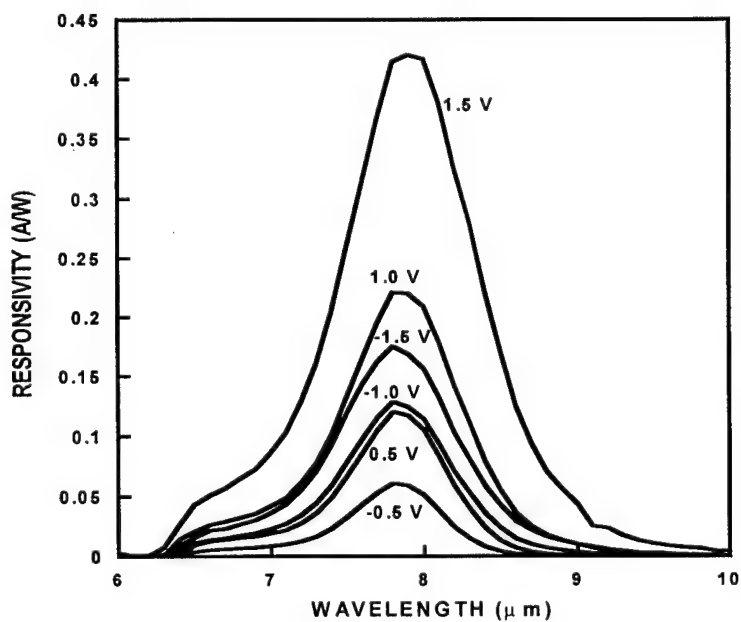


Figure 3.2.4 Responsivity versus wavelength for the LWIR QWIP-A with normal incidence illumination at 77 K.



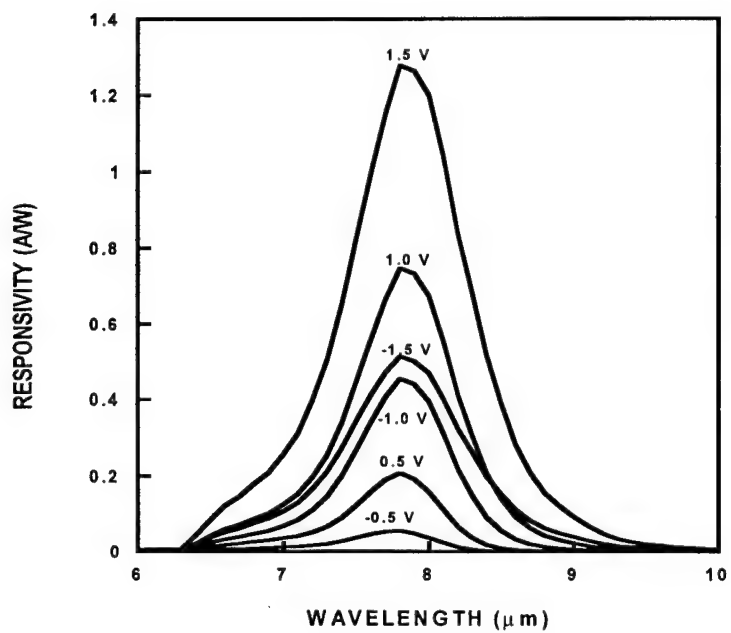


Figure 3.2.5 Responsivity versus wavelength for the LWIR QWIP-A with 45° facet incidence illumination at 35 K.

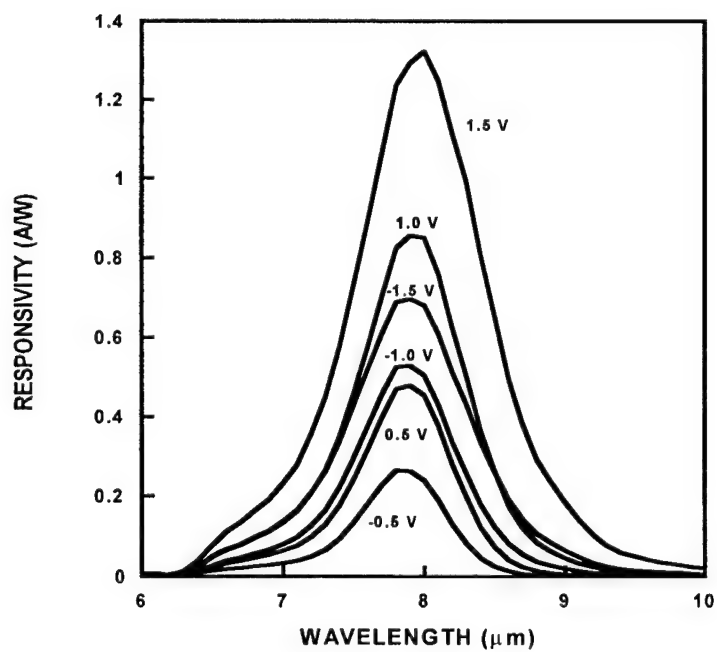


Figure 3.2.6 Responsivity versus wavelength for the LWIR QWIP-A with 45° facet incidence illumination at 77 K.

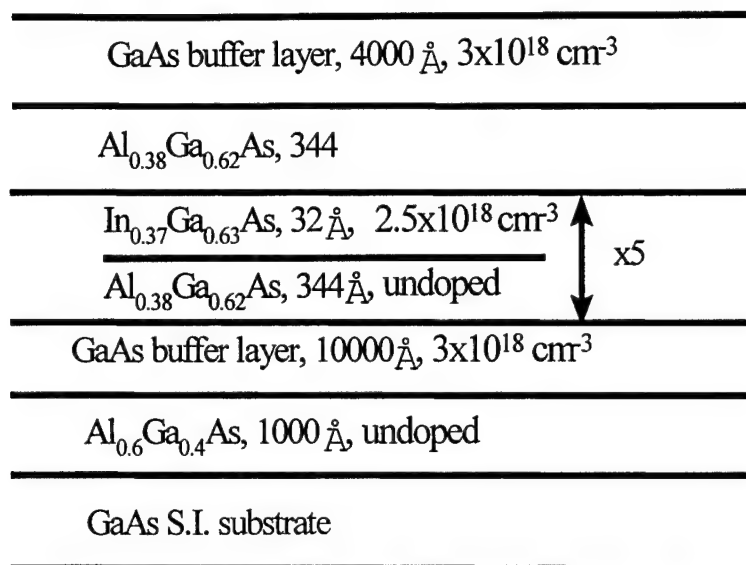


Figure 3.2.7 Layer structure of the MWIR QWIP-B.

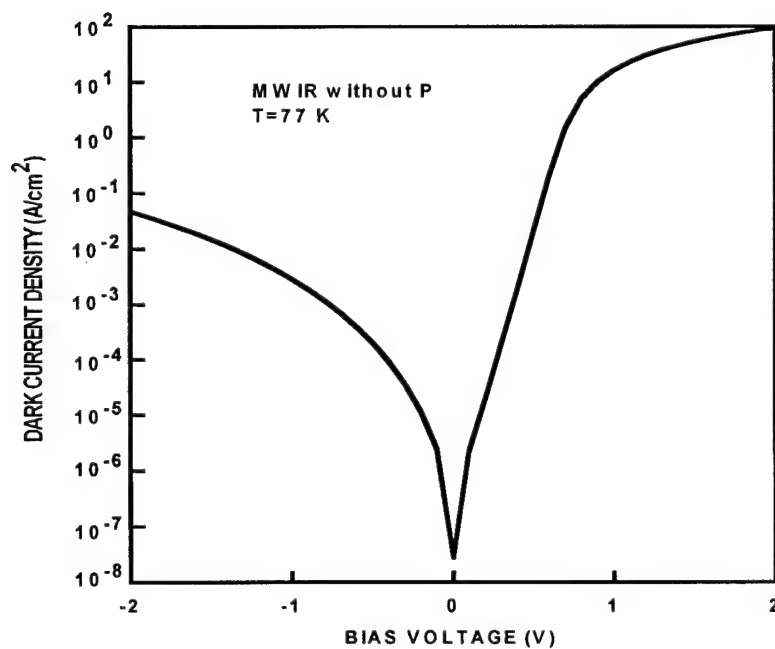


Figure 3.2.8 Dark current density versus bias for the MWIR QWIP-B measured at 77 K.

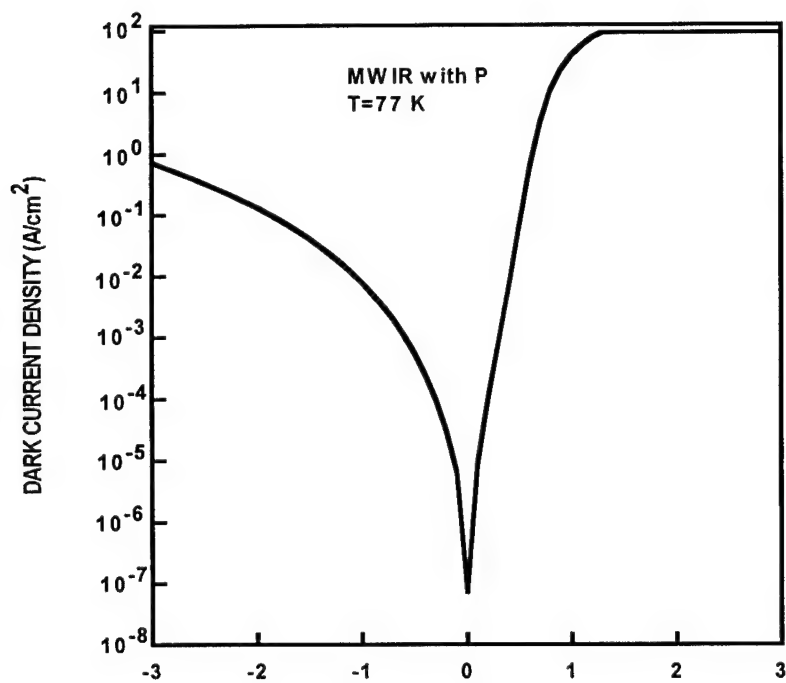


Figure 3.2.9 Dark current density of MWIR QWIP-C at 77 K.

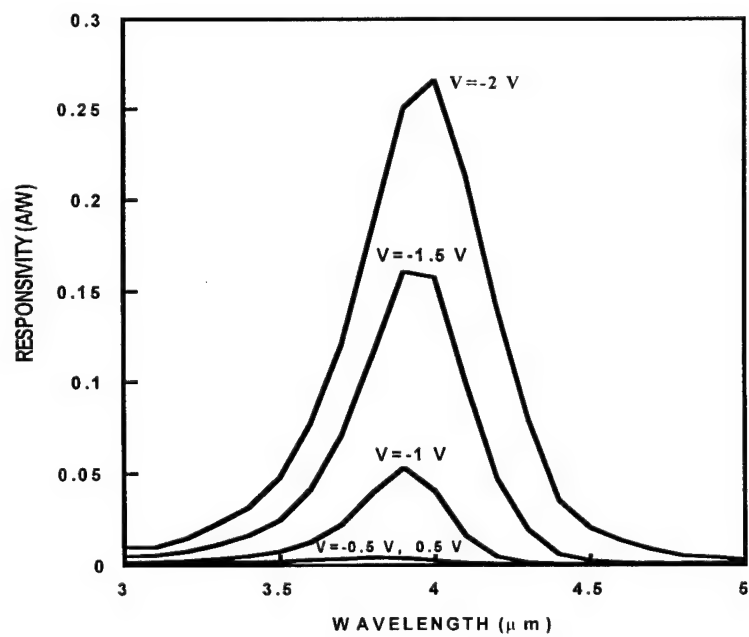


Figure 3.2.10 Responsivity of MWIR QWIP-C under normal incidence at 35 K

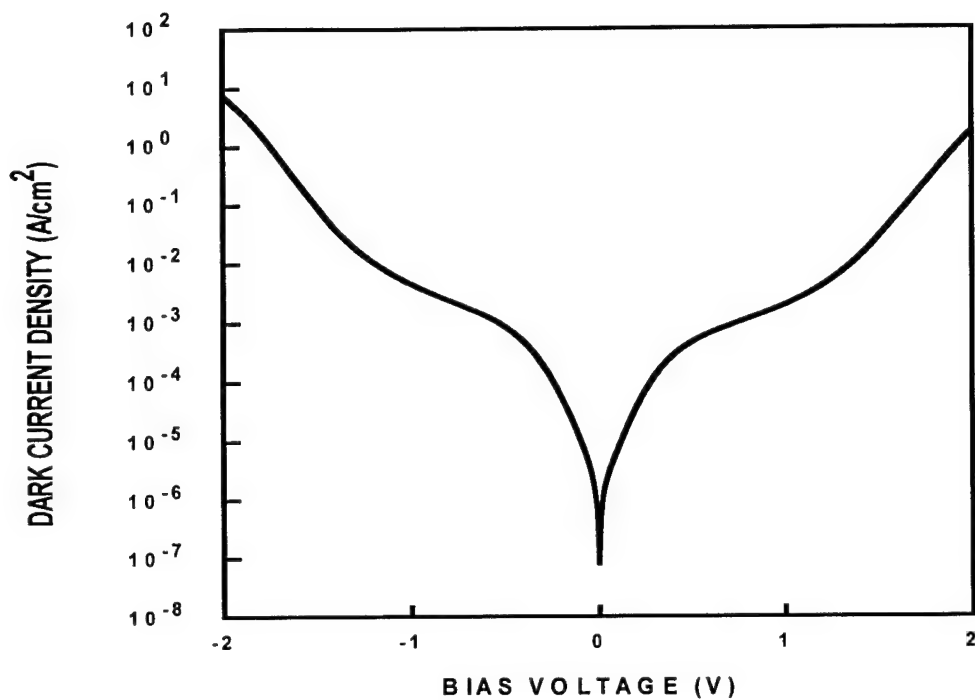


Figure 3.3.1 Dark current density versus bias for QWIP- D measured at 77 K (with no substrate thinning).

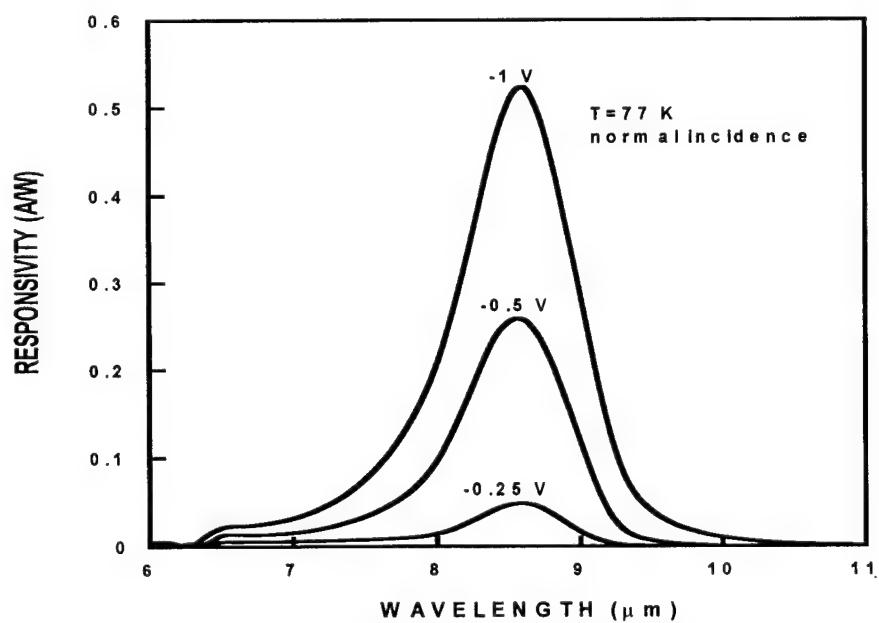


Figure 3.3.2 (a) Responsivity versus wavelength for QWIP- D with normal incidence illumination measured at different biases.

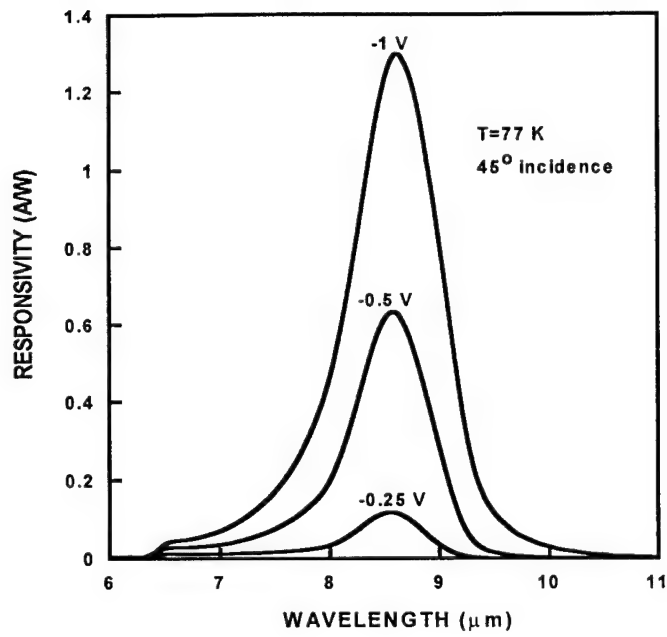


Figure 3.3.2 (b) Responsivity versus wavelength for QWIP- D with  $45^\circ$  incidence illumination at different biases.

## 4. Simplified (S-) QWIPs for Low Temperature and Low Background Applications

### 4.1 Variation of Black Body Flux With Field of View Angle

One important application area for QWIPs is in the situation of low temperature and low background environments. It is important to study the variation of blackbody flux with field of view (FOV) angle. The photon flux  $\phi$  within wavelength range of  $\lambda_1$  and  $\lambda_2$  can be formulated as

$$\phi = \int_{\lambda_1}^{\lambda_2} d\lambda \frac{2\pi c}{\lambda^4} \frac{1}{\exp(\frac{hc}{\lambda k_B T}) - 1} \sin^2 \frac{\Omega}{2} \quad (27)$$

where  $\Omega$  is the FOV angle (see figure 4.1). We have calculated the photon flux within 0-100  $\mu\text{m}$  at different temperatures, and the results are shown in figure 4.2.

### 4.2 Low Temperature and Low Background Modeling for the S-QWIP

The simplified (S-) QWIPs are QWIPs with reduced number of quantum wells (typically less than five) and they offer some unique advantages, such as shorter growth time, higher yield, higher array uniformity *etc.* At low background the device has to be operated at lower temperatures, and it is difficult to achieve BLIP operation at a low background even with reduced operation temperature. It is useful to predict theoretically at what background the device will achieve BLIP operation. Here we consider sample 3 described in section 3.1. Figure 4.3 shows the dark current of this device at 77K and 40K, as well as the 300K window current when the detector is kept at 77K. The dashed lines in figure 4.3 gives the calculated window current with a photon flux of  $7.7 \times 10^{17} \text{ cm}^{-2}\text{s}^{-1}$ ,  $4.5 \times 10^{14} \text{ cm}^{-2}\text{s}^{-1}$  and  $1.1 \times 10^{13} \text{ cm}^{-2}\text{s}^{-1}$ , from top to the bottom, respectively. From this figure

one can see that the device is BLIP at 77K with a 300K background and 36° field of view angle. The top dash line is the calculated 300K background current which matches well with the measured data. When the photon flux is reduced, the device is no longer BLIP at 77K. From the figure one can see that the device is BLIP at 40K with a low background of  $4.5 \times 10^{14} \text{ cm}^{-2} \text{ s}^{-1}$ . When the FOV is reduced as in most of the systems, the background photon flux has to be higher in order for the detector to have BLIP operation.

At low background with a far away target, thermal imaging is very difficult and we usually see an unresolved target with an IR FPA. An infrared system model was used to calculate the target detection range as a function of several detector parameters. Path transmission was assumed to be 1 for simplicity. A dark current density of  $10^{-7} \text{ A/cm}^2$  was used for a detector temperature of 40 K, and  $10^{-4} \text{ A/cm}^2$  was used for 77 K detector temperature. The conversion efficiency is defined as photon absorption quantum efficiency times photoconductive gain. The quantum efficiency is assumed to be 25% while the gain varies to change the conversion efficiency. At 77K, the photoconductive gain is assumed to be equal to dark current noise gain. The integration time is varied to fill half of the charge wells of the ROIC. At 40K, the dark current noise gain is assumed to be 0.2 which is not equal to photoconductive gain. The integration time is set to be 30 ms and the charge wells are not quite filled to half of the wells. The parameters which do not change in the modeling are given in Table 4.2.1.

**Table 4.2.1 Parameters used in the modeling**

Parameters	Value	Units
Target Size	1 x 1	m <sup>2</sup>
Background Flux	1x10 <sup>13</sup>	photons/cm <sup>2</sup> /sec
Window Temperature	40	K
Optics Temperature	40	K
Cold Shield Temperature	40	K
Peak Wavelength	8.6	μm
Spectral Bandwidth	1.5	μm
Pixel Size / Pixel Pitch	38 / 40	μm
Noise Gain	0.2	
Charge Well Capacity	5x10 <sup>7</sup>	Electrons
False Alarm Rate	1x10 <sup>-16</sup>	
Signal to Noise Ratio	4.8	
Probability of Detection	50	%

The background flux is chosen to be 1x10<sup>13</sup> photons/cm<sup>2</sup>/sec which is not in BLIP condition. When the target is maintained at the same temperatures, lower background photon flux will give a longer detection range. For 40 K operation, the dark current and the multiplexer (MUX) noises are about half/half, assuming the MUX noise is 300 electrons. At 77 K, the dark current noise dominates. The target temperatures are set at 240K, 270K and 350 K. The results are given in figure 4.4 in which the detection range is plotted as a function of conversion efficiency. The unresolved target detection range is defined as having a signal to noise ratio of 4.8 and probability of detection 50%. A regular QWIP gives a conversion efficiency between 2 to 6 %. When the conversion efficiency increases, the detection range increases as seen in the figure 2. At 40 K, assuming the dark current noise gain is different from the photoconductive gain, a more



significant increase of detection range is achieved than at 77 K where dark current gain is similar to photoconductive gain.

The optics has been assumed to be cooled at 40K which does not contribute to the total noise in the modeling. If the sensor system is not in space and the optics is warm at 300K, 40K operation will have optics noise dominate. The detection range will decrease to similar to 77K operation due to the optics noise. Special readout design to subtract the warm optics current is necessary for long range detection. Another factor is that we have assumed the path transmission as 1 in all cases. When the background is high, the path transmission is smaller than 1. Figure 4.5 gives a basic idea how the path transmission coefficient can dramatically change the detection range.

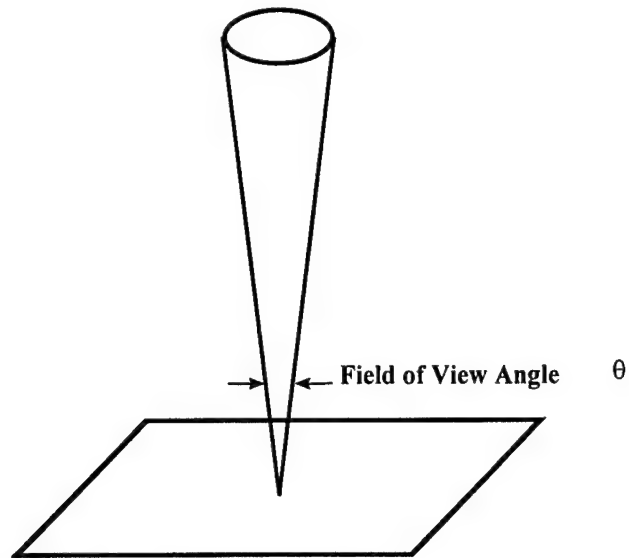


Figure 4.1 Schematic illustration of field of view angle.

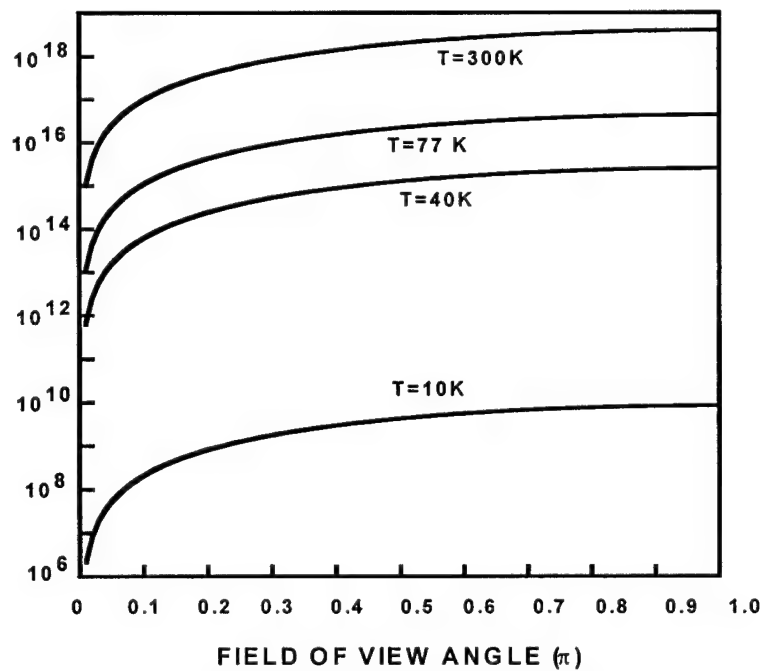


Figure 4.2 Variation of photon flux (photons per unit area per unit time) with field of view angle at different temperatures. The wavelength range under consideration is from 0 to  $100\text{ }\mu\text{m}$ .

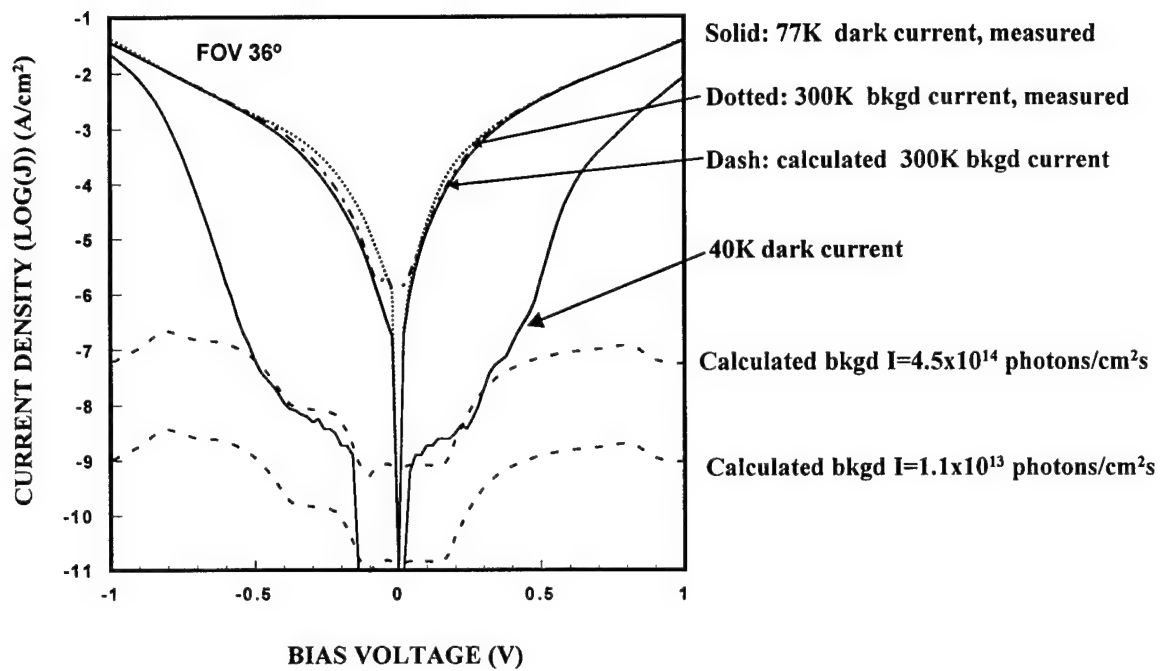
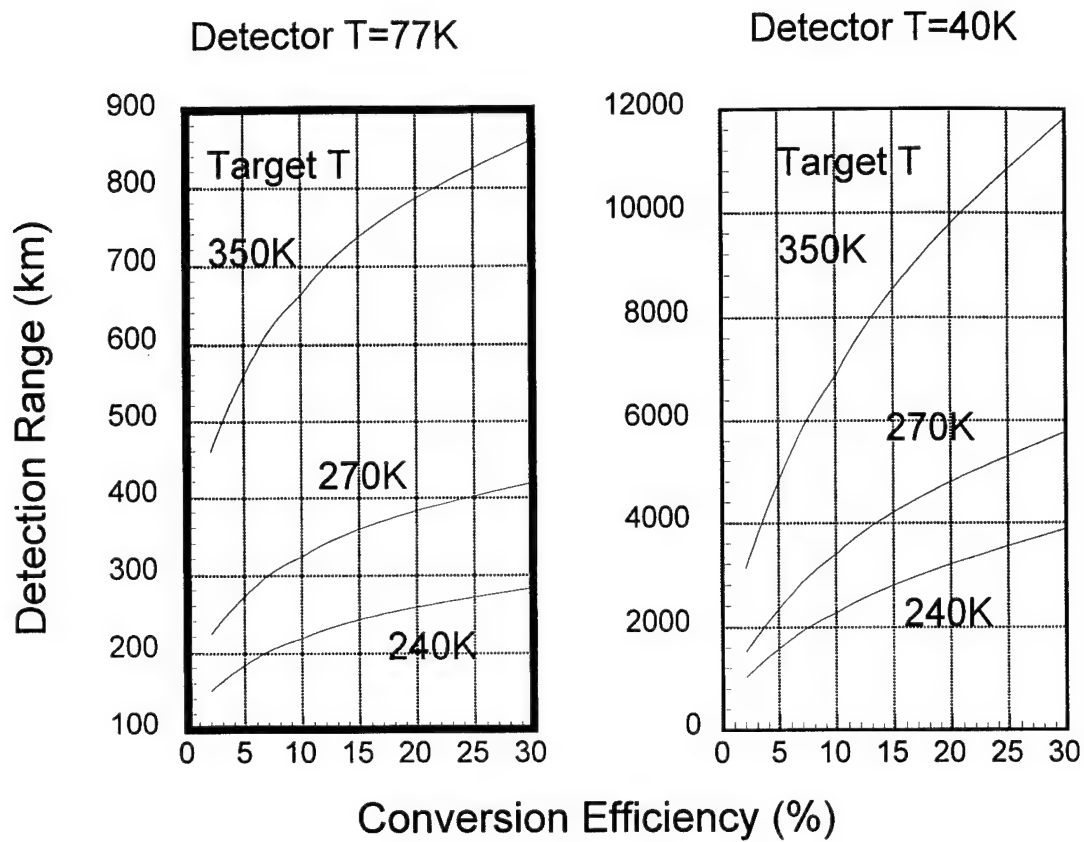


Figure 4.3 The dark current and window photocurrent of a three-well S-QWIP with calculated window photocurrent at different background photon fluxes.



**Figure 2.** The detection range vs. conversion efficiency at target temperatures of 240 K, 270 K and 350 K.

Figure 4.4

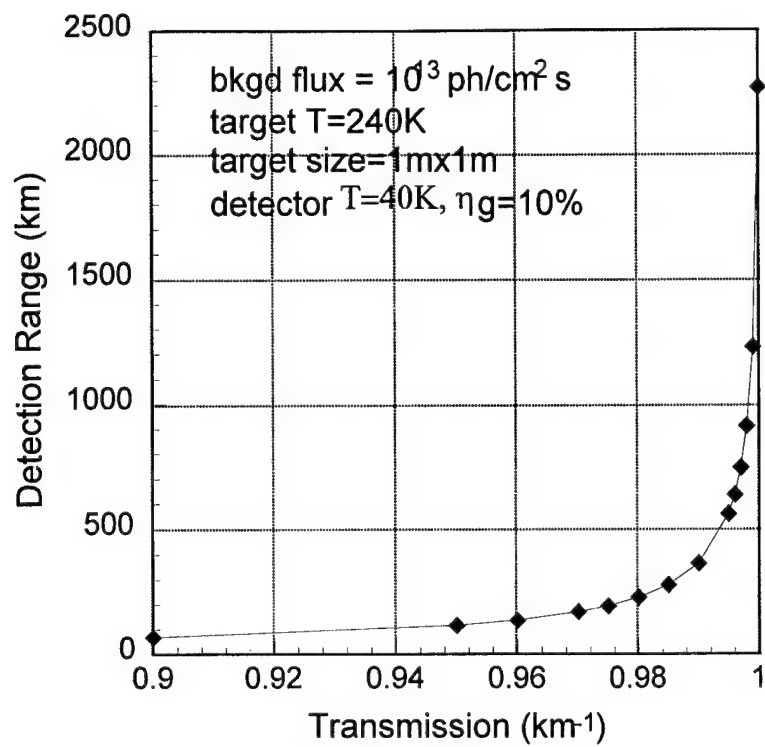


Figure 4.5 The detection range as a function of path transmission.

## 5. A Novel Four- Stack Four- Color QWIP for MWIR and LWIR Applications

### 5.1 Introduction

Recently there is an increasing interest in the development of multi-color QWIPs for MWIR and LWIR dual band detection. Development of a QWIP focal plane array (FPA) for staring image sensor with both MWIR and LWIR spectral bands on single chip is a very important step in meeting the needs and technological challenges of future imaging applications, including space exploration and sensing systems, medical imaging and basic scientific research. Two common approaches have been used to achieve multi-color detection. One common approach is to employ coupled quantum wells which is voltage-tunable to realize multi-color detection [37,38]. However, the wavelength tunability is usually quite small. Another approach uses the stacked structure consisting of two (or more) stacks of QWIPs with one MWIR stack and one LWIR stack grown on the semi-insulating GaAs substrate. In this way one can realize simultaneous detection of MWIR and LWIR wavebands. Employing this type of structure, Tidrow *et al.* have made a high quality two-stack, two-color QWIP for MWIR and LWIR detection[20].

The simplified QWIP (S-QWIP) discussed earlier usually contains quantum wells of less than ten periods, whereas the conventional QWIPs contain 40 to 50 periods of active quantum wells. The S-QWIP has many advantages, such as reduced material growth time and high yield, easier array fabrication, low bias and hence lower power consumption, easier to realize multi-color in a stacked structure *etc.* These advantages have made the S-QWIP very attractive for multi-color multi-stack QWIP applications. A three-well QWIP has been demonstrated which shows very high performance [36]. A

very unique feature about S-QWIP is that the optical gain of it is very large compared to that of long - period QWIPs due to the reduced transit time of photo-excited electrons. This makes S-QWIPs very useful for low photon background detection.

The schematic energy band diagram of the 4-color QWIP device is shown in figure 5.1. It consists of two stacks of multiple quantum wells as the active region with a highly doped contact layer in between them. The first stack is designed to detect one LWIR and one MWIR, the LWIR structure consists of eight periods of a 600 Å  $\text{Al}_{0.27}\text{Ga}_{0.73}\text{As}$  barrier and a 55 Å GaAs well, the doping density is  $0.7 \times 10^{18} \text{ cm}^{-3}$ ; the MWIR structure consists of four periods of a 400 Å  $\text{Al}_{0.38}\text{Ga}_{0.62}\text{As}$  barrier and a 35 Å  $\text{In}_{0.22}\text{Ga}_{0.78}\text{As}$  well, the doping density is  $2.8 \times 10^{18} \text{ cm}^{-3}$ . The second stack is designed to detect two different LWIRs, the first LWIR structure consists of five periods of a 500 Å  $\text{Al}_{0.25}\text{Ga}_{0.75}\text{As}$  barrier and a 50 Å GaAs well, the doping density is  $0.6 \times 10^{18} \text{ cm}^{-3}$ ; the second LWIR structure consists of ten periods of a 800 Å  $\text{Al}_{0.16}\text{Ga}_{0.84}\text{As}$  barrier and a 65 Å GaAs well, the doping density is  $0.4 \times 10^{18} \text{ cm}^{-3}$ . The middle contact is made of 4000 Å GaAs and the doping density is  $1 \times 10^{18} \text{ cm}^{-3}$ . The sample was grown on semi-insulating (100) GaAs by molecular beam epitaxy (MBE) using  $\text{As}_2$  as the arsenic source.

The sample was processed into devices with area of  $216 \times 216 \mu\text{m}^2$  using standard photolithography and wet chemical etching. The mesa structures of the top stack and whole stack were formed by etching down from the top contact layer to the middle contact layer and to the bottom contact layer, respectively. The mesa structure of the bottom stack was formed first by completely removing the top contact and the top stack, and then etching down from the middle contact layer to the bottom contact layer. Ohmic

contact was made by depositing a square contact ring composed of AuGe/Ni/Au on the periphery of the mesa. The device substrate was polished to have a 45° facet for IR illumination. No substrate thinning was made on this device. In the dark current and photoresponse measurements, the bottom contact layer was grounded and top (middle) contact layers were positively or negatively biased. The photoresponse was measured by back illumination using a monochromator and a calibrated blackbody source.

## **5.2 Device Performance and Characteristics**

### **5.2.1 The top stack**

Figure 5.2 shows the dark current density of the top stack. The solid lines are dark current densities measured at 40K, 60K, 77K and 90K and the dashed line is the measured 300K window current density with a 180° FOV. The BLIP temperature was found to be 60K up to  $\pm 2.5$ V.

Figure 5.3(a) shows the responsivity of top stack at 40K under several different bias. Two peaks were observed, one at 9.0  $\mu\text{m}$  and another one at 12.3  $\mu\text{m}$ . At  $\pm 1.5$ V and  $\pm 1$ V, two peaks appear simultaneously while at  $\pm 3$ V only the 12.3  $\mu\text{m}$  peak shows up with a responsivity larger than 2 A/W. The full width at half-maximum (FWHM) for both peaks are around 1.3  $\mu\text{m}$ . Figure 5.3(b) shows the peak responsivities at 9.0  $\mu\text{m}$  and 12.3  $\mu\text{m}$  versus bias voltage at 40K. The responsivities at both peak wavelengths increase initially with applied voltage and after reaching a maximum value, the responsivity with peak wavelength at 9.0  $\mu\text{m}$  drops continually. The responsivity with peak wavelength at 12.3  $\mu\text{m}$  first reaches a maximum value, then drops continually, after reaching a



minimum value it increases again. One can see from this figure that the two peak responsivities exhibit an interesting competition with applied voltage.

When the temperature is increased to 77K, the 12.3  $\mu\text{m}$  response peak is almost not observable, as can be seen from figure 5.4(a) which shows the peak responsivities versus applied voltage. This is due to the fact that at 77K the thermionic emission dark current for the 12.3  $\mu\text{m}$  peak is too large, which prevents the photocurrent to be observed at this temperature. Figure 5.4(b) shows the spectral responsivity of the top stack at 0.5V and -0.5V bias and 77 K. As can be seen from this figure, only the 9.0  $\mu\text{m}$  peak appears. Compared to the 40K spectral responsivity, the peak position does not change but the responsivity increases at 77K.

### 5.2.2 The bottom stack

Figure 5.5 shows the dark current density of the bottom stack at several different temperatures along with the 300K window current density with 180° FOV. The BLIP temperature was found to be 77K up to  $\pm 5$  V.

Figure 5.6(a) shows the LWIR responsivity of bottom stack at 3V and -4V bias, and 77K. The peak wavelength is found to be at 8.5  $\mu\text{m}$  under both biases. At 3V, the cut-on full width at half-maximum (FWHM) is at 8.1  $\mu\text{m}$  and cutoff FWHM at 9.3  $\mu\text{m}$  with a spectral bandwidth of 1.2  $\mu\text{m}$ . At -4V, the cut-on FWHM is at 8.1  $\mu\text{m}$  and cutoff FWHM at 9.0  $\mu\text{m}$  with a spectral bandwidth of 0.9  $\mu\text{m}$ . Figure 5.6(b) shows the dependence of peak responsivity on the applied voltage. As can be seen from this figure, the peak responsivity increases with bias. We have also measured the LWIR responsivity of the bottom stack at 77K, they show a similar result as at 40K. Figure 5.7(a) shows the LWIR

spectral responsivity of the bottom stack at 77K with bias of 3V and -4V. Figure 5.7(b) shows the bias dependence of the peak responsivity. Compared to the 40K case, there is an increase in the responsivity at 77 K.

Figure 5.8(a) shows the MWIR responsivity of the bottom stack at 77K under two different biases, 2V and -2V. The response peak for this MWIR stack is at  $4.7\text{ }\mu\text{m}$ . The FWHM is about  $0.5\text{ }\mu\text{m}$ . Figure 5.8(b) shows the bias dependence of peak responsivity. As can be seen from this figure, the peak responsivity increases with bias up to +2V under positive bias and -2.5V under negative bias, and becomes saturated with a maximum value of  $0.46\text{ A/W}$  at 2V. The spectral responsivities at  $\pm 2\text{V}$  bias at 90K are shown in figure 5.9(a), and the peak responsivity dependence on bias at 90K is shown in figure 5.9(b), respectively. At 90K, the responsivity under negative bias is slightly larger than that under the corresponding positive bias.

### 5.2.3 The MWIR-LWIR stacked QWIP

The dark current density of the whole MWIR-LWIR stacked is shown in figure 5.10. As can be seen from this figure, the device is under BLIP at 77K with bias up to  $\pm 7\text{V}$ . Figure 5.11(a) shows the LWIR responsivity of the whole stack at 40K under several different biases. Two response peaks at  $8.8\text{ }\mu\text{m}$  and  $12.3\text{ }\mu\text{m}$  were observed in the whole stack QWIP. FWHM for both peaks are around  $1.3\text{ }\mu\text{m}$ . It is noted that there are two LWIR QWIPs contributed to the  $8.8\text{ }\mu\text{m}$  peak, one at the top stack with peak wavelength at  $9.0\text{ }\mu\text{m}$  and the other at the bottom stack with peak wavelength at  $8.5\text{ }\mu\text{m}$ . The interaction between these two peaks at a certain bias results in the observed  $8.8\text{ }\mu\text{m}$  peak. Figure 5.11(b) shows the peak responsivity versus applied bias. As can be seen

from this figure, they exhibit a similar competition phenomena as we have already seen in the top stack case. Also similar to the top stack case, when the temperature is increased, the 12.3  $\mu\text{m}$  peak cannot be observed due to the very large thermionic emission dark current at high temperatures. Figure 5.12(a) shows the LWIR responsivity of the top stack at 77K under two different biases, 7V and -6V. Figure 5.12(b) shows the bias dependence of the 8.8  $\mu\text{m}$  peak responsivity at 77K.

Figure 5.13(a) shows the MWIR responsivity of the whole stack at 77K under two different biases, 3V and -6V. The peak wavelength is also at 4.7  $\mu\text{m}$ . At both biases the cut-on FWHM is at 4.35  $\mu\text{m}$  and the cutoff FWHM is at 4.95  $\mu\text{m}$  with a spectral bandwidth of 0.9  $\mu\text{m}$ . The dependence of peak responsivity on bias at 77K is shown in figure 5.13(b). The peak responsivity increases linearly with bias up to  $\pm 3$  V and becomes saturated with a maximum value of 1 A/W at 3V. Figure 5.14(a) shows the MWIR spectral responsivity of the whole stack at 2V and 3V. Figure 5.14(b) shows the bias dependence of the peak responsivity at 90K. They show a similar characteristics as the 77K case.

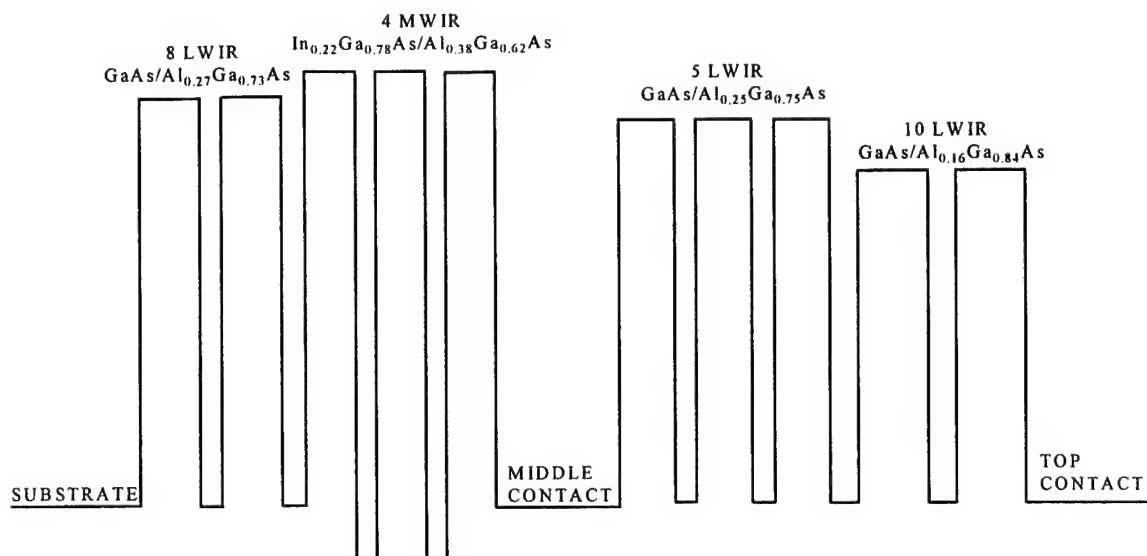


Figure 5.1 Schematic energy diagram of the four-stack, four-color QWIP.

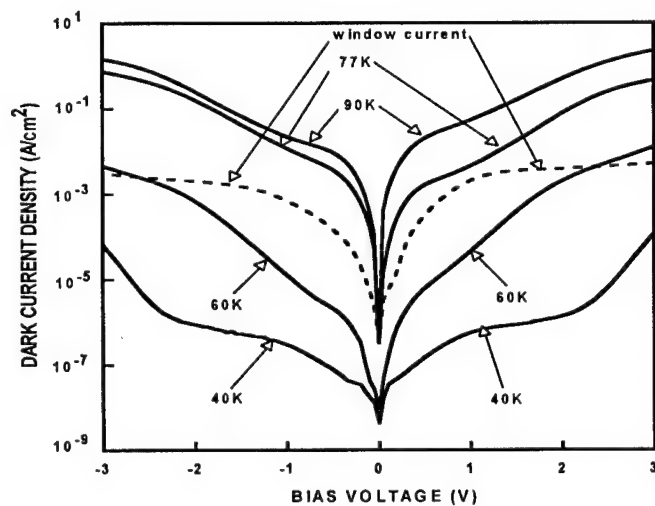


Figure 5.2 Dark current density versus bias for the top stack.

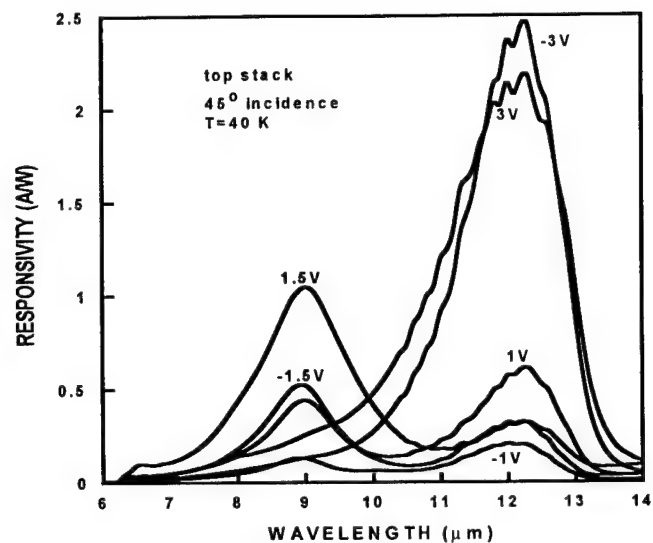


Figure 5.3(a) Responsivity of the top stack at 40K.

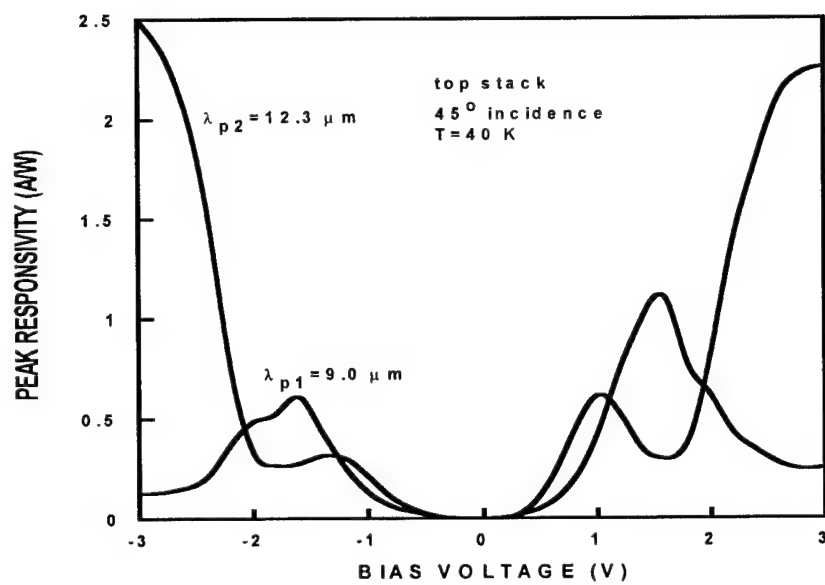


Figure 5.3(b) Peak responsivity versus applied voltage for the top stack at 40K

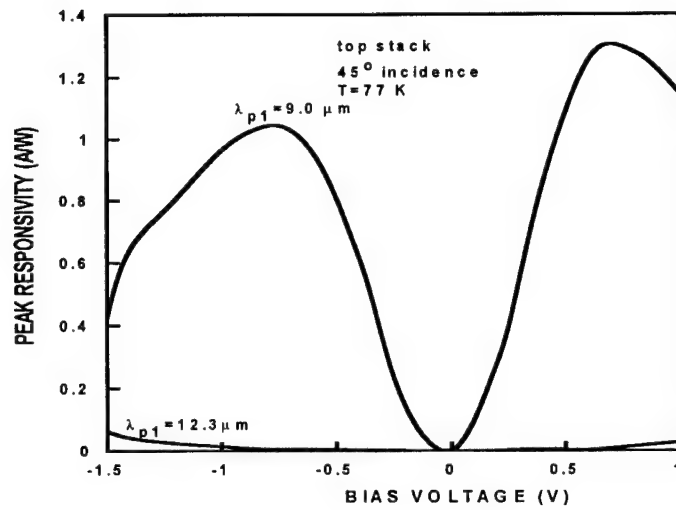


Figure 5.4(a) Peak responsivity versus applied voltage for the top stack at 77K.

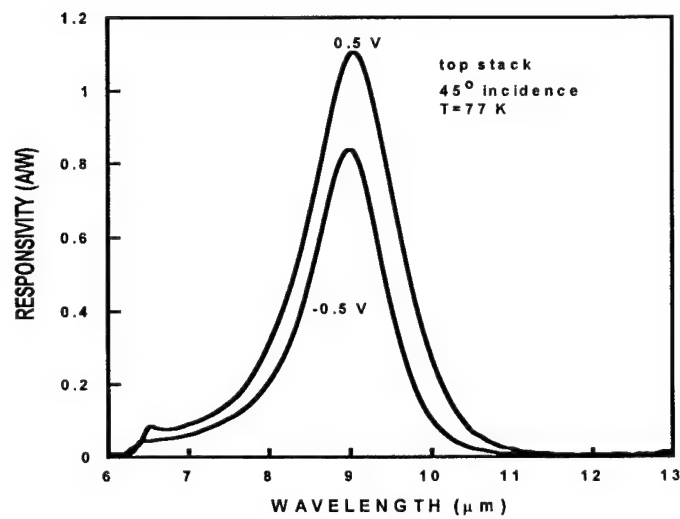


Figure 5.4(b) Responsivity of the top stack at 77K.

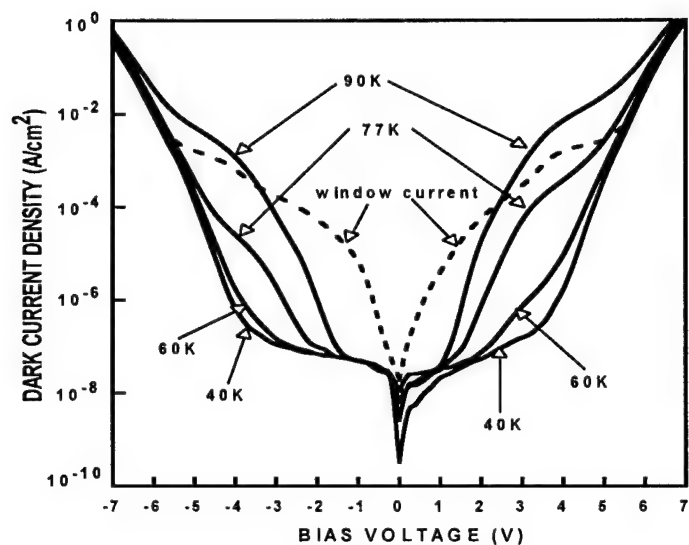


Figure 5.5 Dark current density of the bottom stack.

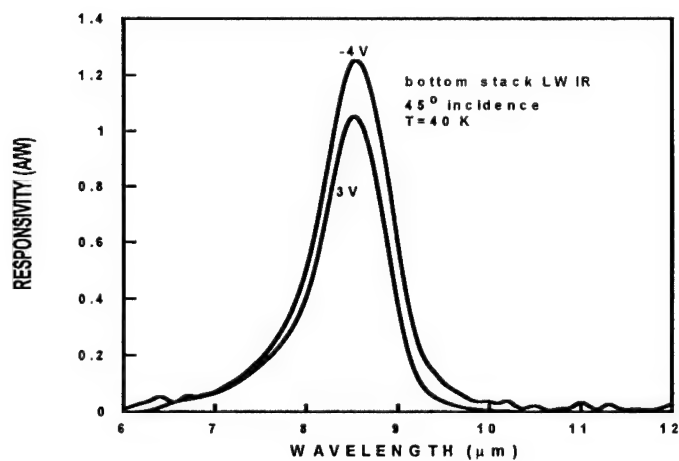


Figure 5.6(a) LWIR responsivity of the bottom stack at 40K.

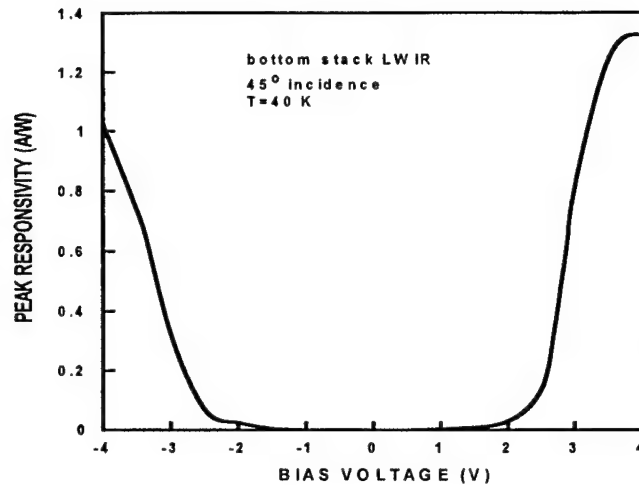


Figure 5.6(b) LWIR peak responsivity of the bottom stack at 40K.

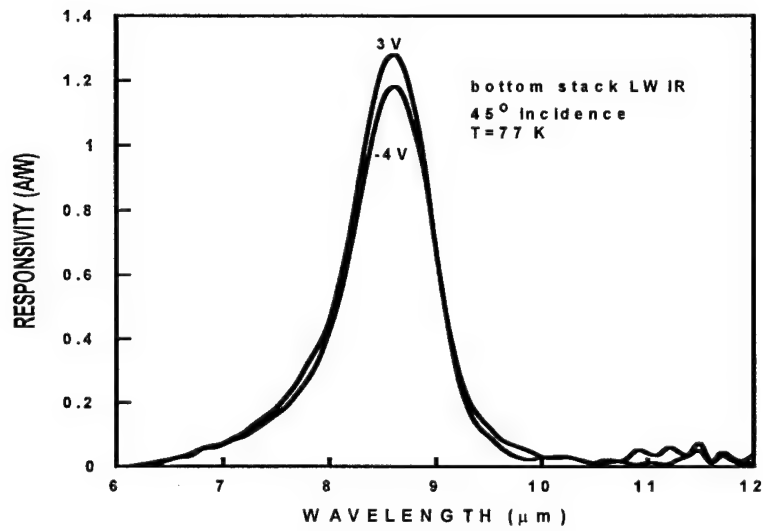


Figure 5.7(a) LWIR responsivity of the bottom stack at 77K.



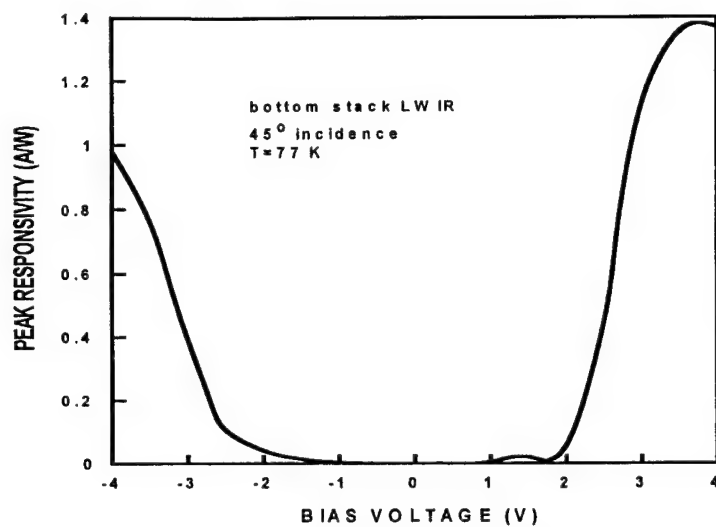


Figure 5.7(b) LWIR peak responsivity versus applied voltage at 77K.

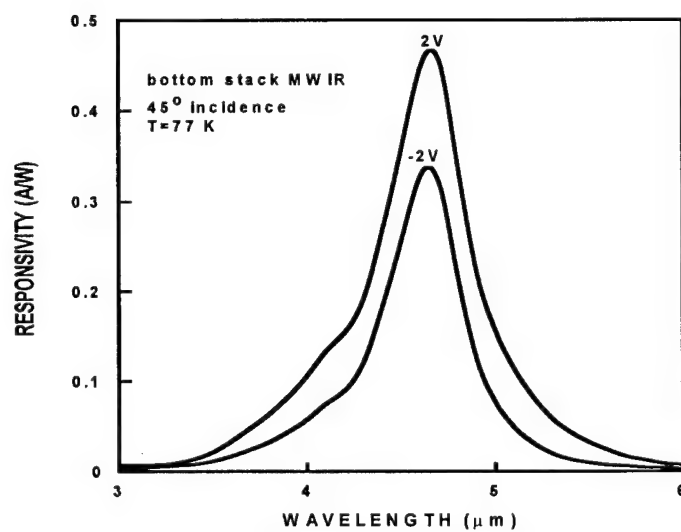


Figure 5.8 (a) MWIR responsivity of the bottom stack at 77K.

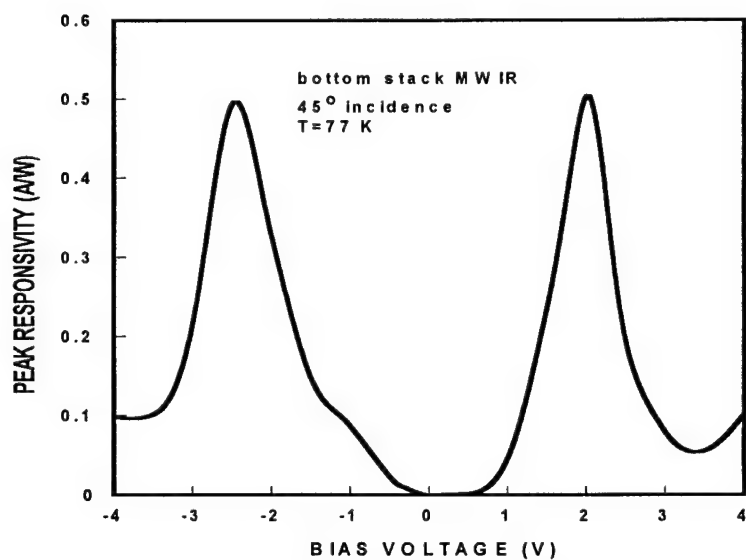


Figure 5.8(b) MWIR peak responsivity versus applied voltage for the bottom stack at 77K.

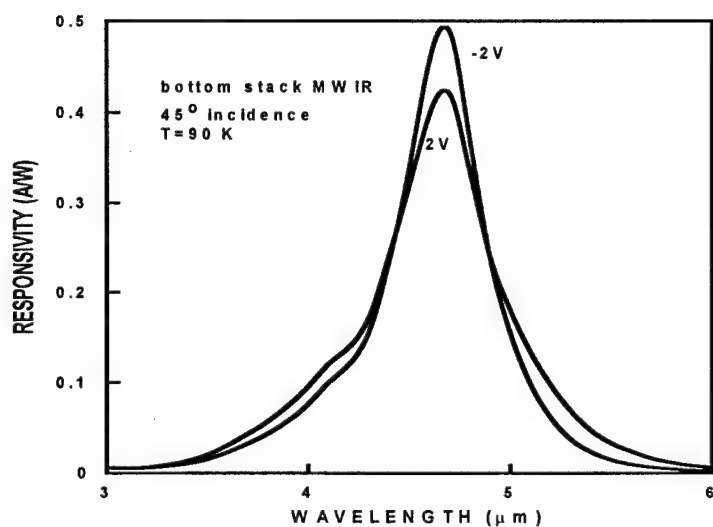


Figure 5.9(a) MWIR responsivity of the bottom stack at 90K.

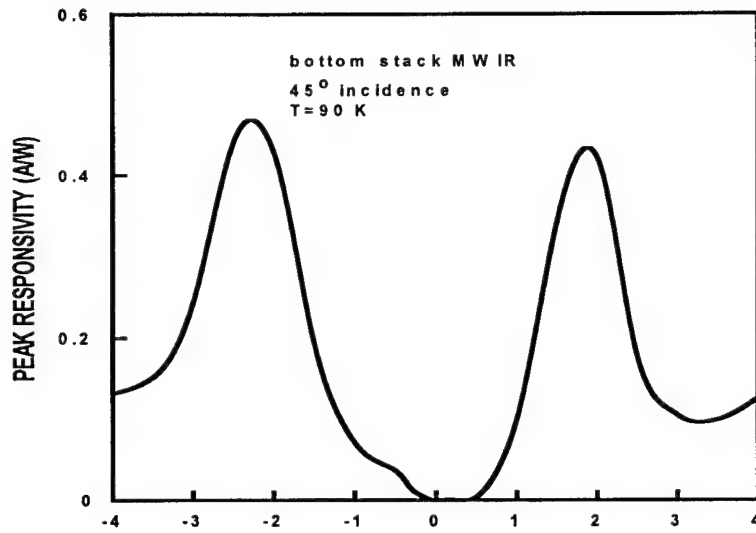


Figure 5.9(b) MWIR peak responsivity versus applied voltage at 90K.

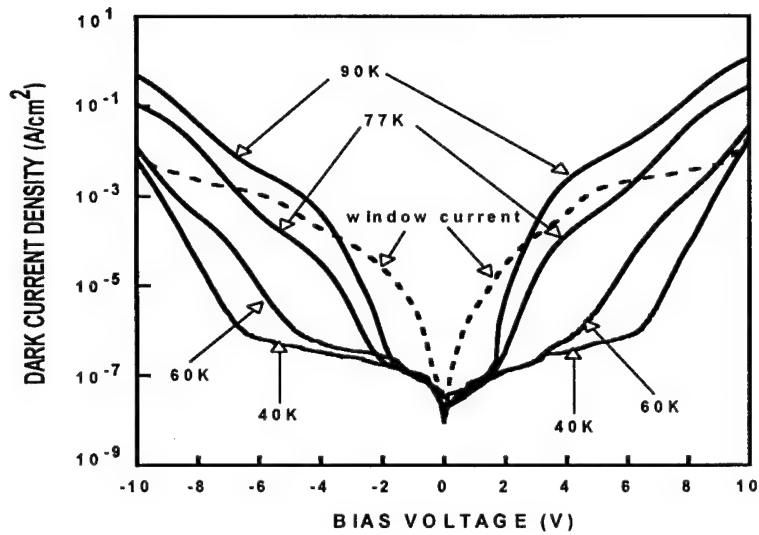


Figure 5.10 Dark current density of the whole stack.

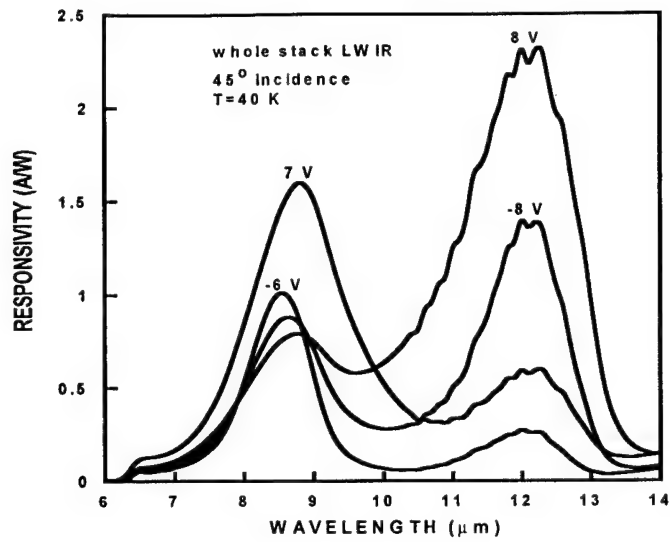


Figure 5.11 (a) LWIR responsivity of the whole stack at 40K.

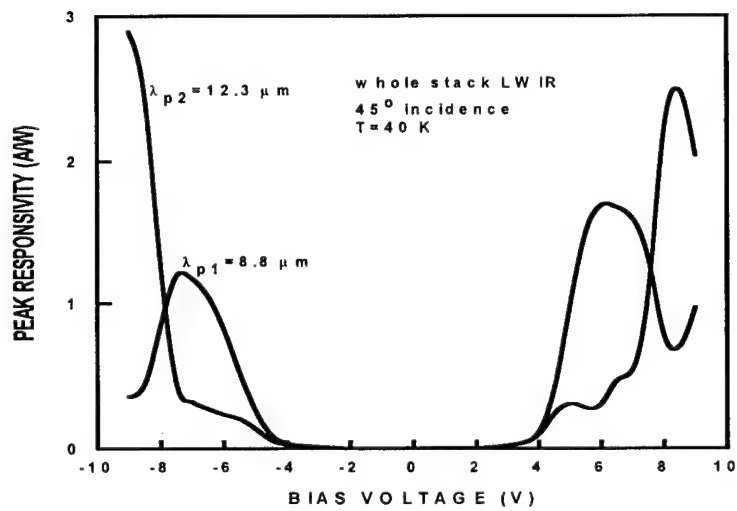


Figure 5.11 (b) LWIR peak responsivity versus applied voltage for the whole stack at 40K.

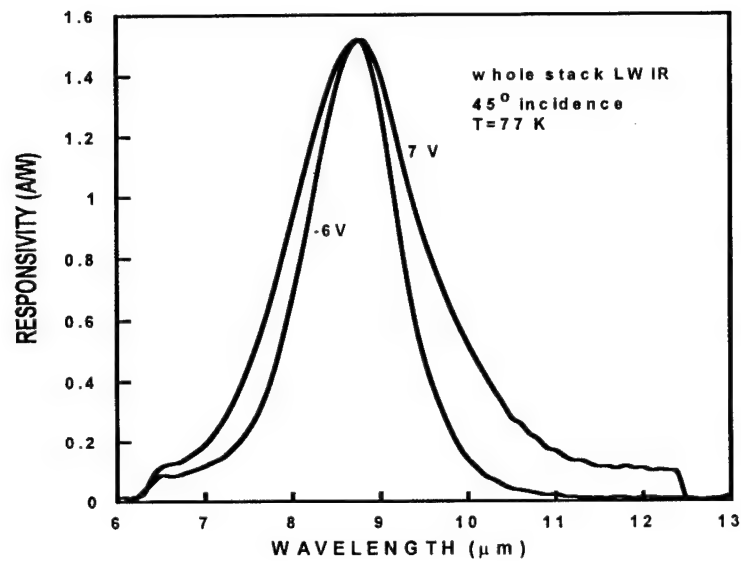


Figure 5.12(a) LWIR responsivity of the whole stack at 77K.

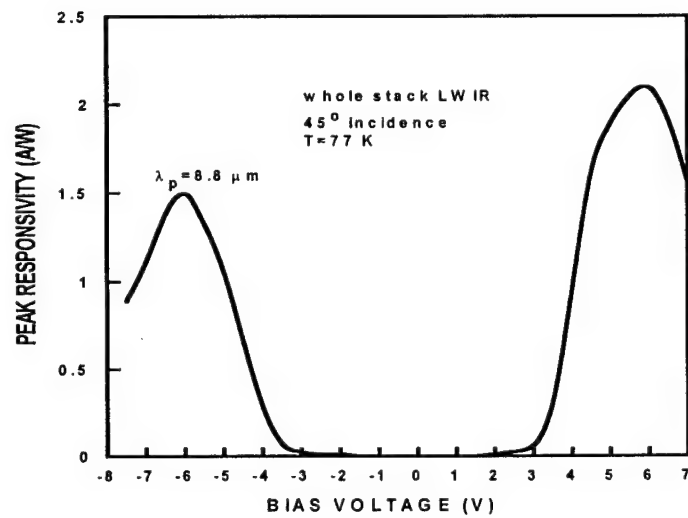


Figure 5.12 (b) LWIR peak responsivity versus applied voltage for the whole stack at 77K.

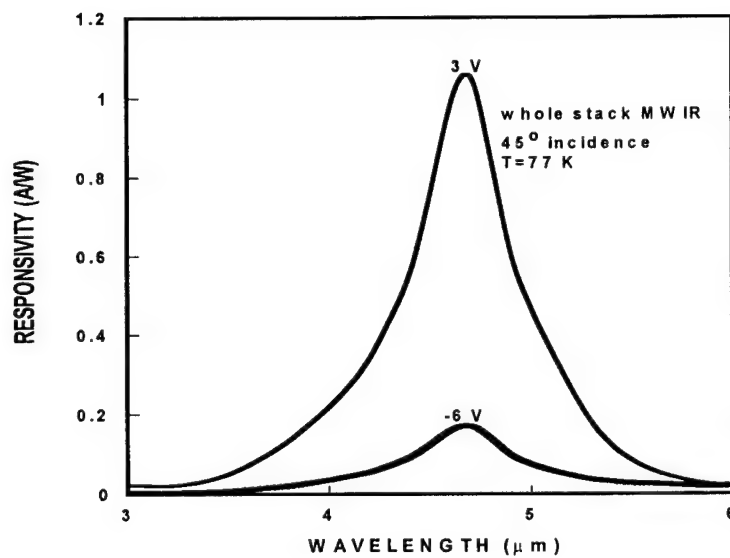


Figure 5.13(a) MWIR responsivity of whole stack at 77K.

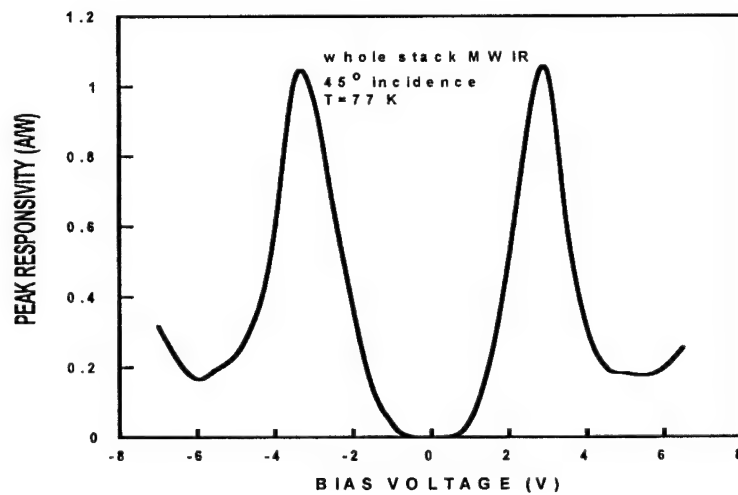


Figure 5.13(b) MWIR peak responsivity versus applied voltage of the whole stack at 77K.

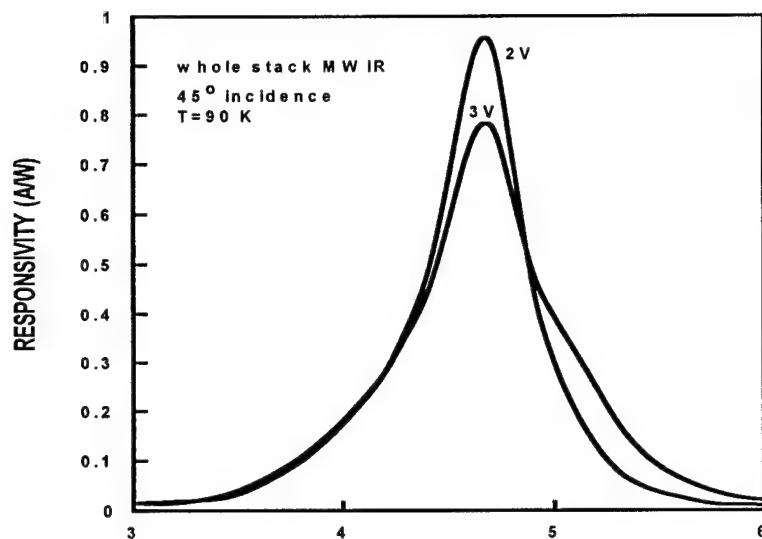


Figure 5.14(a) MWIR responsivity of the whole stack at 90K.

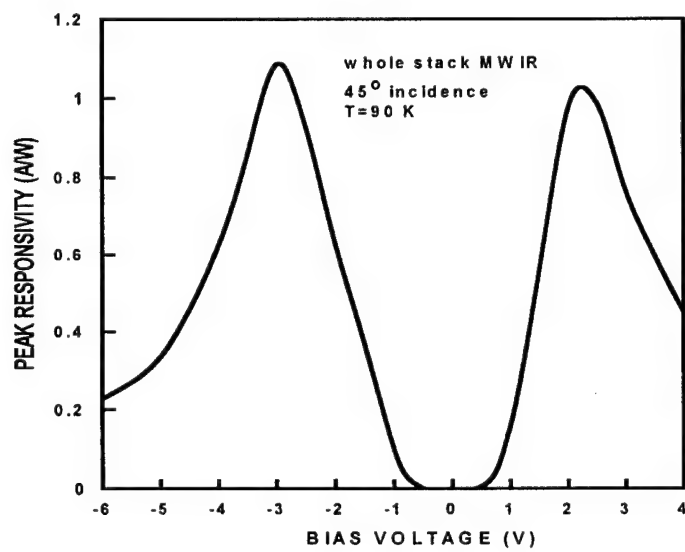


Figure 5.14(b) MWIR peak responsivity versus applied voltage at 90K.

## 6. Quantum Confined Stark Effect in an Asymmetric Weakly Coupled Double Quantum Wells Structure

### 6.1 Introduction

Two common approaches have been used to achieve multicolor detection. One approach uses the stacked structure consisting of two (or multi) stacks of QWIPs with one MWIR stack and one LWIR stack grown on the SI GaAs substrate. Employing this kind of structure, Tidrow *et al.* made a high quality two-stack, two-color QWIP [21]. Another common approach is to employ the coupled QW structure which is voltage-tunable to realize multicolor detection [37,38]. This wavelength tunability is very useful in military application such as target discrimination. From the point of view of physics, voltage-tuning is associated with the motion of confined electrons and holes under an electric field along the confined direction. In this case the quantum confined Stark effect is a very important issue. Study on the quantum Stark effect will help to design new novel multicolor QWIPs.

In general Stark shift refers to the shift of energy levels of a charge system under an applied electric field. There have been extensive study on quantum confined Stark effect in quantum wells [39-47]. Stark shift in a single quantum well is very small [39]. To increase the Stark shift, a high electric field is needed and this will induce large leakage current in optical modulators and dark current in QWIPs. Stark shift in a step quantum well structure has also been studied [40] and it shows a very large Stark shift compared to the single quantum well under the same bias. Other structures have also been suggested to further enhance Stark shift. It is very desirable to have a large Stark shift under low bias for the practical applications of the Stark shift QWIP structures.



In this section we describe an asymmetric weakly coupled double quantum wells structure which can have very large Stark shift under very low bias. As schematically shown in figure 6.1, it consists of a shallow well and a deep well separated by a thin barrier and confined by two thick barriers. The barriers are consisted of  $\text{Al}_{0.3}\text{Ga}_{0.7}\text{As}$  and the shallow well is composed of  $\text{Al}_{0.2}\text{Ga}_{0.8}\text{As}$ . The deep well is composed of GaAs and doping is made in this well with a doping density of  $7 \times 10^{17} \text{ cm}^{-3}$ . In our discussion the conduction band offset parameter  $Q_c$  is taken as 0.55 and all the parameters used in the calculation can be found in [32].

## 6.2 Formulation

The wave function for an electron moving in a quantum well can be written as

$$\Psi(r) = \frac{1}{\sqrt{S}} u_c(r) e^{ik \cdot r_{\parallel}} \phi(z) \quad (28)$$

where  $S$  is the area of the well,  $k$  is the wave vector of the electron in the  $x$ - $y$  plane,  $r_{\parallel}$  is the position vector in the  $x$ - $y$  plane and  $u_c(r)$  is the cell periodic function near the conduction-band extremum,  $\phi(z)$  is the envelope function in the  $z$ - (growth) direction. The Schrödinger equation for  $\phi(z)$  in the presence of an electric field  $F$  (as shown in Fig. 6.1(b)) is

$$-\frac{\hbar^2}{2} \frac{d}{dz} \left( \frac{1}{m_j^*(z)} \frac{d\phi(z)}{dz} \right) + (V_j - eFz)\phi(z) = E\phi(z) \quad (29)$$

where  $m_j^*$  is the effective mass of electron in the  $j$ -th layer,  $V_j$  is the potential in  $j$ -th layer,  $E$  is the energy of electron associated with the motion in  $z$ - direction. The double wells system can be biased in two different ways. For the electric field shown in figure

6.1(b) we call it under negative bias. In each layer  $m_j^*$  is a constant and has a sharp change at the interface. The variation of effective at the interfaces has a significant effect on the electronic properties of the quantum well system. Within each layer Eq. (29) can be rewritten as

$$-\frac{\hbar^2}{2m_j^*} \frac{d^2 \phi(z)}{dz^2} + (V_j - eFz)\phi(z) = E\phi(z) \quad (30)$$

By transforming into a dimensionless coordinate  $Z$ ,

$$Z = -\left(\frac{2m_j^*}{(e\hbar F)^2}\right)^{1/3} (E - V_j + eFz) \quad (31)$$

Equation (30) becomes

$$\frac{d^2}{dZ^2} \phi(Z) - Z\phi(Z) = 0 \quad (32)$$

The solution of this equation can be written as

$$\phi(Z) = a A_i(Z) + b B_i(Z) \quad (33)$$

where  $A_i$  and  $B_i$  are the Airy functions [48]. The boundary conditions are that  $\phi(z)$  and  $m_j^* \frac{1}{L} d\phi(z)/dz$  are continuous at each interface.

When calculating the positions of the energy levels, the exchange interaction energy in the ground state should be taken into account, which can be expressed as [49]

$$E_{exch} = -\frac{e^2}{2\varepsilon} \int_0^{k_f} \frac{d^2 k'}{(2\pi)^2} \int dz \int dz' \frac{e^{-|k-k'||z-z'|}}{|k-k'|} |\phi_1(z')|^2 |\phi_1(z)|^2 \quad (34)$$

where  $k_f = (2\pi\sigma)^{1/2}$ ,  $\sigma$  is the two-dimensional electron density in the quantum well,  $\varepsilon$  is the dielectric constant,  $k$  and  $k'$  are the in-plane wave vectors of electrons. Under usual doping condition, the exchange energy will lower the ground state subband energy by 5

to 10 meV and shift the absorption peak to shorter wavelength. The direct interband Coulomb interaction (repulsive) is much smaller than the exchange energy and can be neglected.

Considering an optical transition from initial state 1 to final state 2 in the quantum well, the oscillator strength  $f$  associated with this transition is

$$f = \frac{2}{m_w^*} \frac{\left| \langle \phi_2 | p_z | \phi_1 \rangle \right|^2}{E_2 - E_1} \quad (35)$$

where  $m_w^*$  is the effective mass of electron in the well and  $p_z$  is the momentum operator of electron in the  $z$  - direction. The absorption coefficient of a system is proportional to the oscillator strength and joint density of states. Oscillator strength plays an important role in determining the optical properties of a system.

The absorption coefficient can be obtained from Fermi's golden rule and the result is

$$\alpha(\omega) = \frac{4\pi^2 e^2}{nc\omega} \int_{BZ} \frac{2d^3k}{8\pi^3} P_{12}^2 [f(E_1) - f(E_2)] \frac{\Gamma_{12}}{\pi} \frac{1}{(E_2 - E_1 - \hbar\omega)^2 + \Gamma_{12}^2} \quad (36)$$

where  $n$  is the refractive index,  $\omega$  is the incident light frequency,  $E_1$  and  $E_2$  are the energies of the initial and final states, respectively.  $f(E)$  is the Fermi-Dirac distribution functions.  $\Gamma_{12}$  is a broadening parameter. The momentum matrix element  $p_{12}$  is

$$p_{12} = -\frac{i\hbar}{m_w^*} \langle \phi_2 | \frac{\partial}{\partial z} | \phi_1 \rangle \quad (37)$$

We will use the following formula for the Fermi energy

$$E_F = k_B T \left( \exp\left(\frac{N_D}{n_0}\right) - 1 \right) + E_1 \quad (38)$$

where  $k_B$  is the Boltzmann's constant,  $N_D$  is the doping density and  $n_0 = 4\pi m_w^* k_B T / h^2 L_w$ ,  $T$  is the temperature,  $h$  is the Planck's constant and  $L_w$  is the well width.

We next consider the device performance of this structure. For practical applications of quantum well system for QWIPs, we are concerned with the dark current and responsivity of the structure. In order to calculate the dark current, we need to consider the tunneling probability of a quantum well. Assuming that the well width is  $L_w$  and the barrier width is  $L_b$ , the effective mass of electron is  $m_w^*$  in well and  $m_b^*$  in barrier and the barrier height is  $E_b$ , then under a bias  $F$ , the tunneling probability can be obtained from the WKB approximation and the results yields

$$T(E, F) = \begin{cases} 1, & E > E_b - eF L_w \\ \exp\left(-\frac{4}{3\hbar eF} (2m_b^*)^{1/2} (E_b - E - eF L_w)^{3/2}\right), & E_b - eF(L_w + L_b) < E < E_b - eF L_w \\ \exp\left(-\frac{4}{3\hbar eF} (2m_b^*)^{1/2} \left\{ (E_b - E - eF L_w)^{3/2} - (E_b - E - eF(L_w + L_b))^{3/2} \right\}\right), & E_1 < E < E_b - eF(L_w + L_b) \end{cases} \quad (39)$$

Under negative bias, the dark current density  $J_d$  can be obtained as

$$J_d = \frac{e m_{wr}^*}{\pi \hbar^2 L_p} \frac{\mu_r F}{\sqrt{1 + (\mu_r F / v_{sr})^2}} \int_{E_1}^{\infty} f(E) T_r dE + \frac{e m_{wl}^*}{\pi \hbar^2 L_p} \frac{\mu_l F}{\sqrt{1 + (\mu_l F / v_{sl})^2}} \int_{E_2}^{\infty} f(E) T_l dE \quad (40)$$

where  $m_{wr}^*$  and  $m_{wl}^*$  are the effective masses of electrons in the right well and left well, respectively,  $\mu_r$  and  $\mu_l$  are the mobility for electrons in the right and left wells, respectively,  $v_{sr}$  and  $v_{sl}$  are their respective saturated velocities.  $L_p$  is the thickness of the whole structure.  $T_r$  and  $T_l$  are the tunneling probabilities for the right and left wells, respectively.

The peak responsivity  $R_p$  is given by

$$R_p = \frac{e}{h\nu} \frac{1 - \exp(-2\alpha l)}{2} p_e g \quad (41)$$

where  $h\nu$  is the energy of incident light,  $\alpha$  is the absorption coefficient of the QWIP,  $l$  is the length of high field domain in QWIP,  $p_e$  is the escape probability of electrons from the well and  $g$  is the optical gain.

We will use the formula developed in this section to study the Stark effect in the structure shown in figure 6.1 and discussed its device performance.

### 6.3 Results and Discussion

In the following discussion, we shall first show how the structure parameters affect the energy levels and oscillator strength, then we will choose a particular parameter and discuss the Stark effect and finally we will discuss the device performance.

#### 6.3.1 Variation of energy levels and oscillators with structure parameters

There are two bound levels in the proposed QWIP structure, the lower level is from the deep well, and the higher level is from the shallow well. The position of these two levels will be affected by the structure parameters, such as the left well width, thin barrier width and right well width. In our discussion the thick barrier thickness is kept at 300 Å.

Figure 6.2 shows the effect of right well width on the  $E_1$  and  $E_2$  and the oscillator strength associated with the transition between the two levels. In the calculation, the left well width is set to be 70 Å, and the thin barrier thickness is taken to be 30 Å. It is seen from figure 6.2(a) that  $E_1$  decreases rapidly with right well width, while  $E_2$  decreases

slowly. This can be understood from a single quantum well case. It is well known that in a single quantum well, the energy levels decrease with the well width. Since  $E_1$  is originated from the right well which is weakly coupled to the left well, it will be greatly affected by the right well width. Due to the coupling with the right well, the effective left well width will be increased with the right well width, and the  $E_2$  level which is originated from the left well will also decrease correspondingly. It is also seen from figure 6.2(a) that exchange energy will cause the ground state ( $E_1$ ) to be lowered down about 10 meV. The oscillator strength first decreases with the right well width and then almost remains constant and then increases with the right well width. This is because as the right well width begins to increase, the transition energy increases and the overlap of the wave functions of the two states does not increase very much and results in a decrease of oscillator strength. As the right well width continues to increase, the two effects (increase of transition energy and wave functions overlap) are balanced and oscillator strength is almost constant. Further increasing the right well width, the increase of the wave functions overlap becomes dominant, which results in the increase of oscillator strength.

The effect of left well width on the energy levels and oscillator strength is shown in figure 6.3(a) and (b), respectively. In the calculation, the right well and thin barrier widths are taken as 70 Å and 30 Å, respectively. It is seen from figure 6.3(a) that  $E_2$  decreases with left well width, and  $E_1$  is almost not affected. Compared to figure 6.2(a), the decrease of  $E_2$  with left well width is not so significant as the decrease of  $E_1$  with the right well width. This is due to the fact that the barrier height for the left well is significantly smaller than that for the right well. The oscillator strength decreases with the

left well width. This is due to the fact that when the left well width increases, the overlap between the wave functions of two levels decreases and therefore causes the decrease of oscillator strength.

Figure 6.4 show the effect of thin barrier thickness on the energy levels and oscillator strength. In the calculation the right well width and the left well width are taken as 50 Å and 70 Å, respectively. It can be seen from figure 6.4(a) that both of the two energy levels decrease slightly with the increase of the thin barrier. The oscillator strength also decreases with the thin barrier thickness, since increasing the thin barrier thickness the wave function overlap between these two levels will decrease.

It is known from the single quantum well case that more levels will occur when the barrier height is kept constant while increasing the well width. This also happens in this double quantum well structure. For example, an additional level will appear when we increase the right well width to 60 Å and left well width to 100 Å.

### 6.3.2 The effect of electric field

As mentioned before, the transition energy for this QWIP will increase with a blue shift under negative bias condition. The variation of transition energy with applied bias is shown in figure 6.5. As seen from this figure, there is a significant Stark shift in this system with the applied electric field. At zero bias the peak energy for the transition is 108.6 meV while at 20 kV/cm the peak transition energy shifts to 125.8 meV. It is seen that the peak energy will shift 17.2 meV at an applied electric field of 20 KV/cm, which corresponds to a peak wavelength shift of 1.56  $\mu\text{m}$ . The corresponding voltage drop in this double wells structure is 0.15 V at this electric field, which is considered to be quite

low. In the calculation, the right well width, thin barrier thickness and the left well width are taken as 50 Å, 30 Å and 70 Å, respectively.

The wave functions are less sensitive to the applied electric field, as shown in figure 6.6. As seen from figure 6.6(a), the three wave functions for the first bound level under the electric field of 0, 10 and 20 kV/cm are almost indistinguishable. With the increase of applied electric field, the wave function of the second bound level shifts gradually to the right side, which will result in the enhanced overlap of the wave functions of the two levels, as shown in figure 6.6(b). This is consistent with the weak coupling scenario.

As a result of the enhanced overlap of the wave functions of the two levels, the absorption coefficient of the system will increase. We have calculated the absorption coefficient of this system under different biases, and the result is shown in figure 6.7. In the calculation, the broadening parameter is taken as 2 meV. It is clearly seen from this figure that the applied electric field enhances the absorption in the system. It is also noted that due to the smaller overlap between the wave functions of the two levels, the absorption coefficient in this weakly coupled double wells system is significantly smaller than that in the single quantum well bound to bound transition. However, it is still comparable to the single quantum well bound to continuum transitions.

### 6.3.3 Device performance

Tunneling probability is an important quantity in determining the dark current of a QWIP. Figure 6.8(a) and (b) show the tunneling probability of the right and left well,



respectively. It is seen from this figure that with the increase of electric field, the tunneling probability will increase due to the lowering of barrier height. Also, the tunneling probability of the left well is much larger than that of the right well due to the very small thickness of the thin barrier.

The dark current for this QWIP structure was calculated at 77 K and 40 K, and the results are shown in figure 6.9. In the calculation, we have assumed the same mobility and saturation velocity for electrons in both wells, with  $\mu_r = \mu_l = 1000 \text{ cm}^2\text{Vs}^{-1}$  and  $v_{sr} = v_{sl} = 5 \times 10^6 \text{ cm/s}$ , and the device active area is  $210 \times 210 \text{ } \mu\text{m}^2$ . In a conventional bound to bound transition QWIP, the applied bias voltage is usually very high so that electrons can escape efficiently from the quantum well. As a result, large dark current can be expected under high bias condition. In the double quantum wells structure, the second level is close to the barrier height. It can be seen from figure 6.8 that even at a bias of 20 KV/cm, the tunneling probability for both the right well and left well is quite high at  $E_2$  level which means that the electron can tunnel out of quantum wells efficiently. This will result in a reduced dark current compared to the conventional bound to bound transition QWIP.

Figure 6.10 shows the calculated responsivity of this QWIP. In the calculation, the escape probability  $p_e$  is taken to be 0.5, and the optical gain is assumed to be 0.6. The number of quantum well period is taken to be 6 and  $l = 4500 \text{ } \text{\AA}$ . It can be seen from this figure that the responsivity for this QWIP structure is not very high due to the weak coupling of the two wells. However, the wavelength tunability of this QWIP is quite large, which should be useful for the tunable LWIR QWIPs.

The Stark shift effect in an asymmetric weakly coupled double wells system has been depicted in this section. It was shown that the transition peak wavelength of this coupled QWIP structure is very sensitive to the applied electric field. Therefore one can realize large Stark shift with relatively small bias. The overlap of the wave functions of the two bound states is relatively small, but the absorption coefficient of this system is still comparable to that of a bound to continuum transition in a single quantum well.

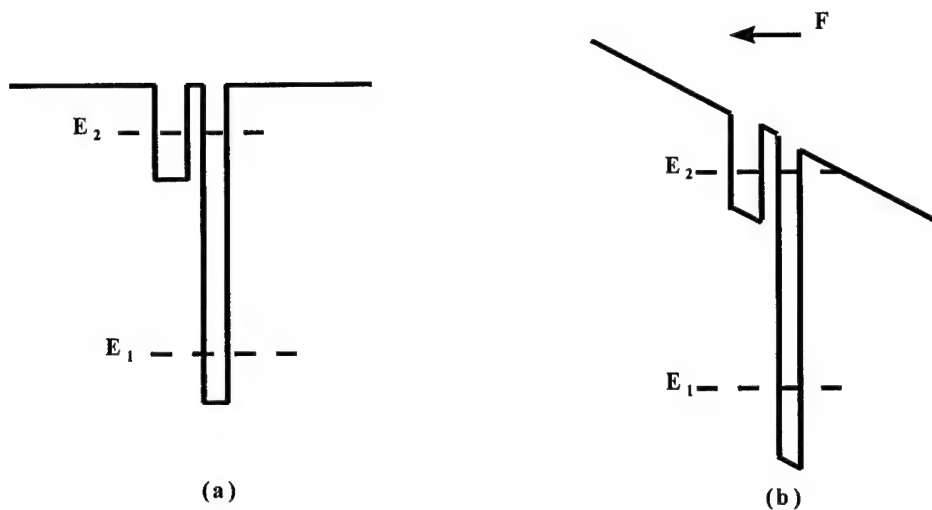


Figure 6.1 Schematic energy band diagrams of the asymmetric weakly coupled double quantum wells at (a) zero bias and (b) negative bias.

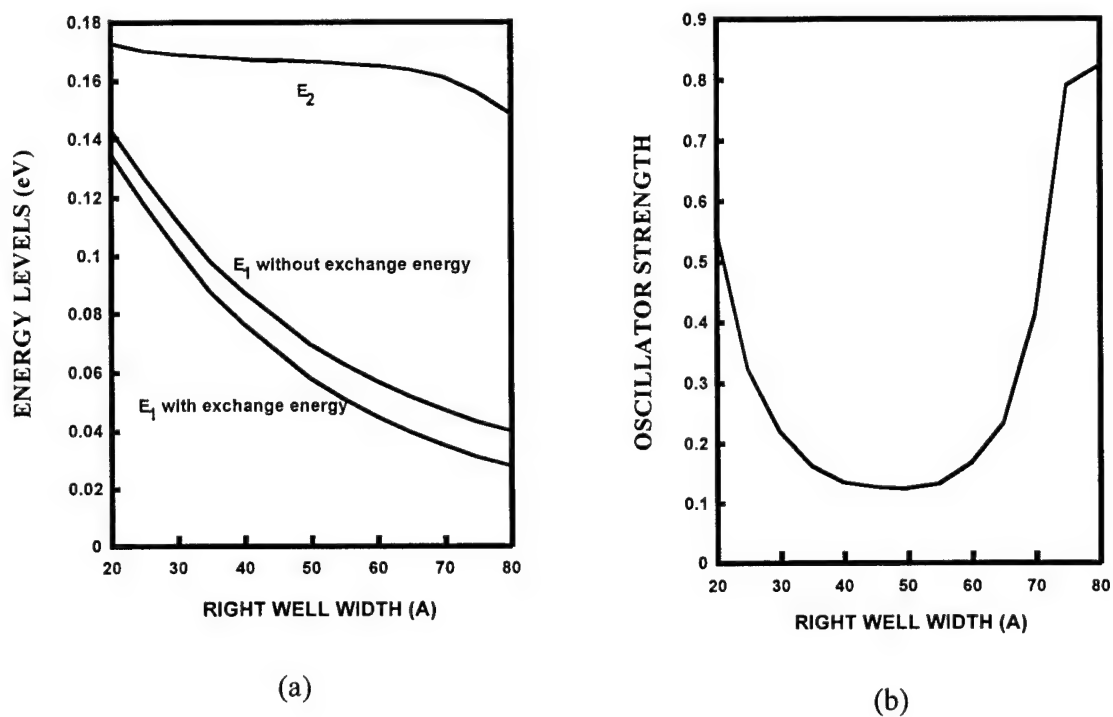
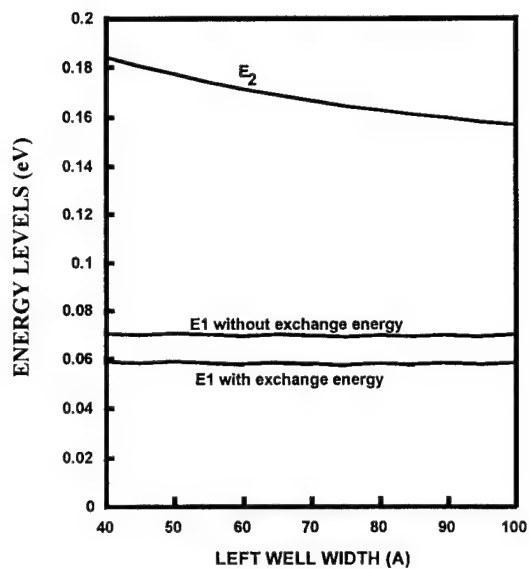
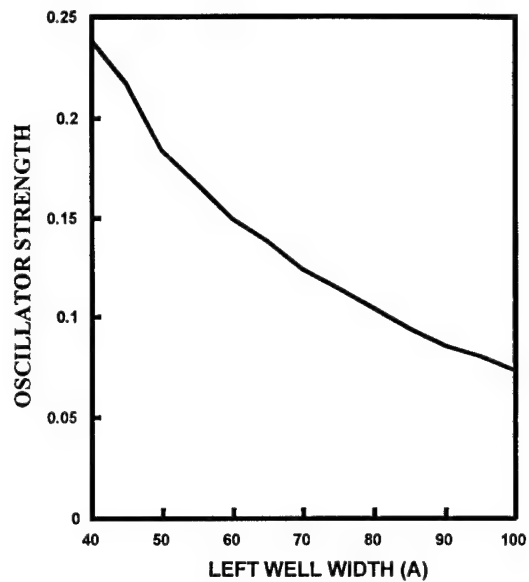


Figure 6.2 Variation of energy levels and oscillator strength associated with the  $E_1$  to  $E_2$  transition with the right well width. The left well width is set to be 70 Å and the thin barrier width is set to be 30 Å.

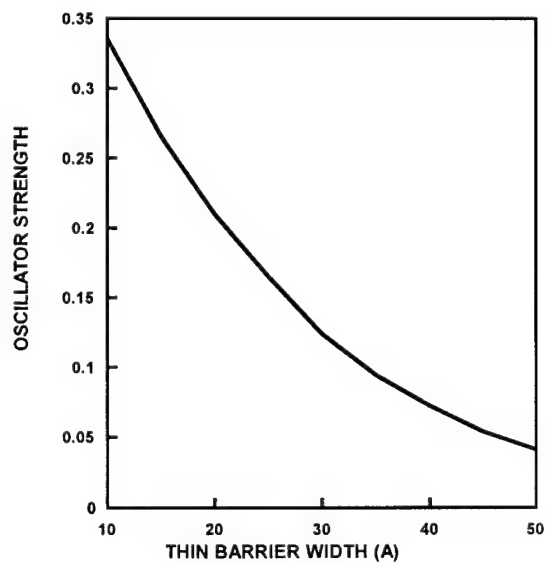
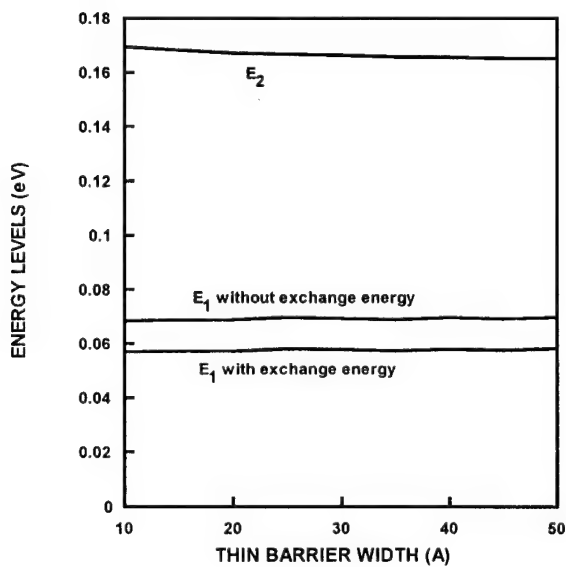


(a)



(b)

Figure 6.3 Effect of left well width on the energy levels (a) and oscillator strength (b). In the calculation the right well width is set to be 50 Å and the thin barrier thickness is set to be 30 Å.



(b)

Figure 6.4 Variation of energy levels and oscillator strength with the thin barrier thickness.

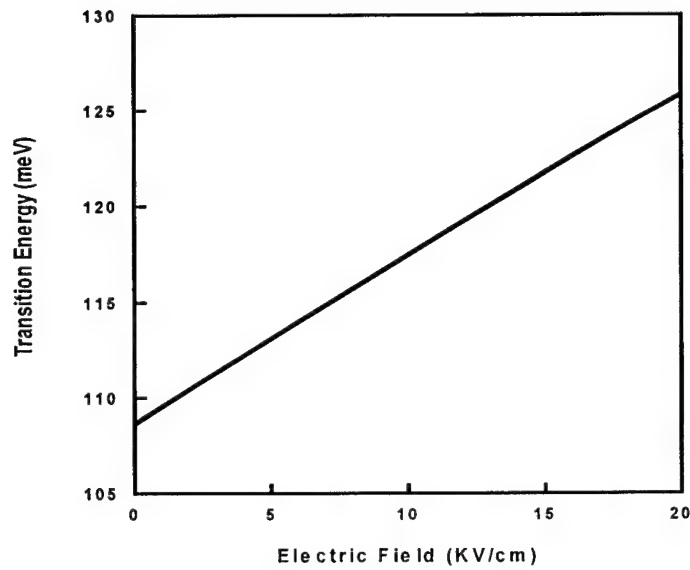


Figure 6.5 Variation of the energy levels with applied electric field. In the calculation, the right well width, thin barrier thickness and left well width are taken as 50 Å, 30 Å and 70 Å, respectively.

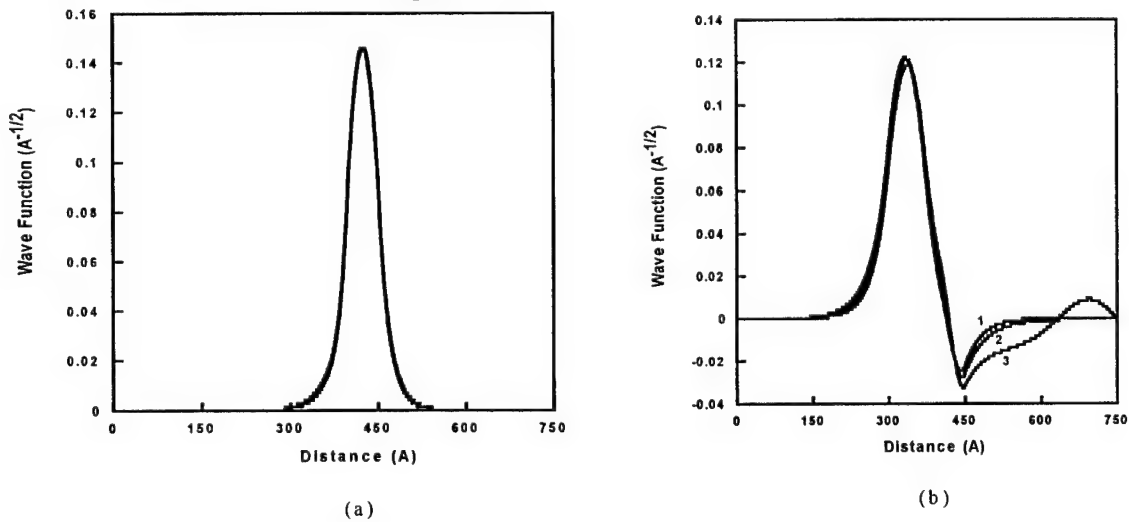


Figure 6.6 Effect of electric field on the wave functions of ground state (a) and excited state(b). In figure 6(a), the ground state wave functions with the applied electric field of 0, 10 and 20 KV/cm are almost indistinguishable. In figure 6(b) the applied electric field is 0, 10 and 20 KV/cm, respectively for the excited state wave functions labeled 1, 2 and 3.

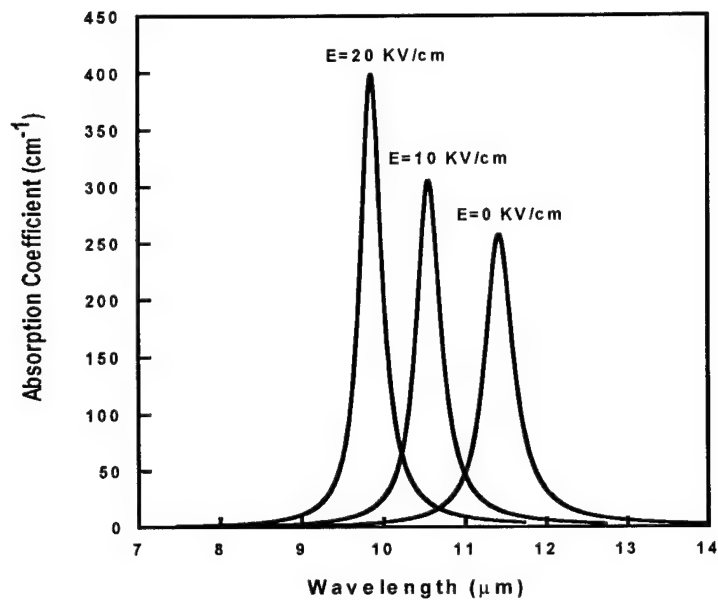


Figure 6.7 Absorption coefficient of the double quantum well system under different electric fields.

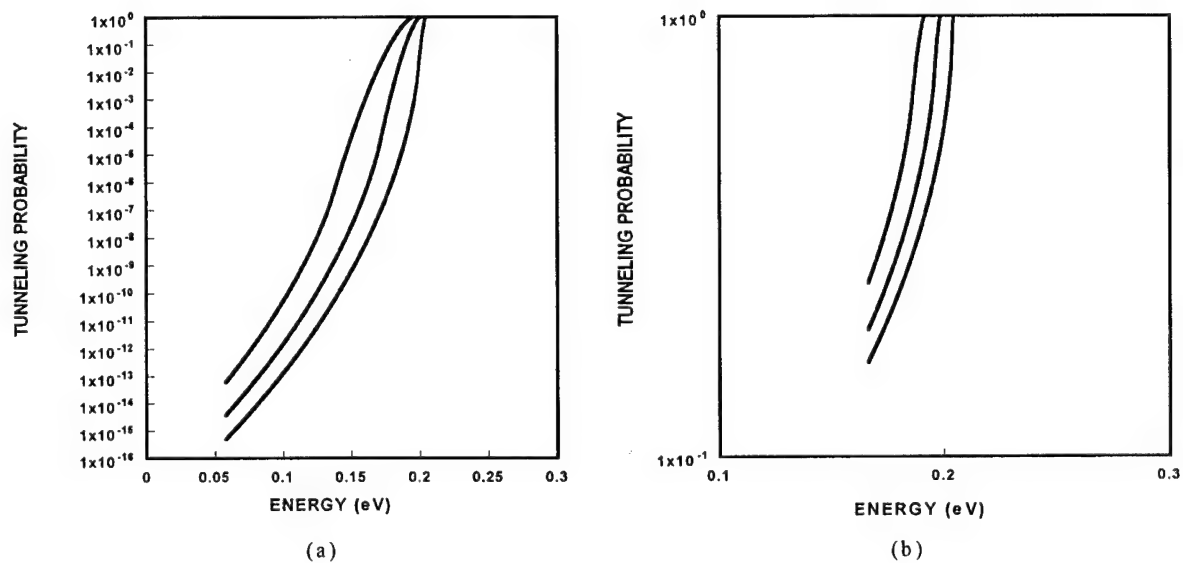


Figure 6.8 Tunneling probability for the right well (a) and the left well (b). In both (a) and (b), the applied electric field are 2, 10 and 20 KV/cm for the curves shown from left to right.

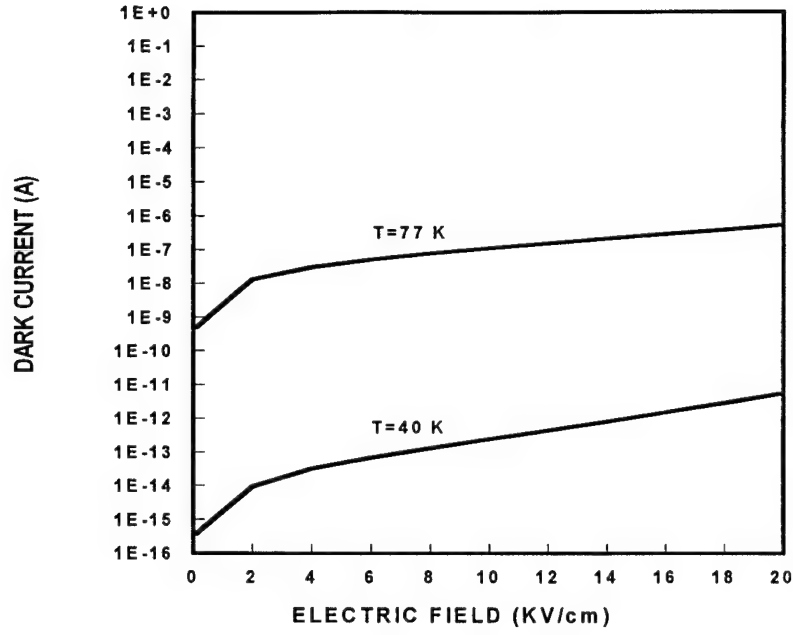


Figure 6.9 Calculated dark current of the double quantum well QWIP structure at T=77 K and T= 40 K.

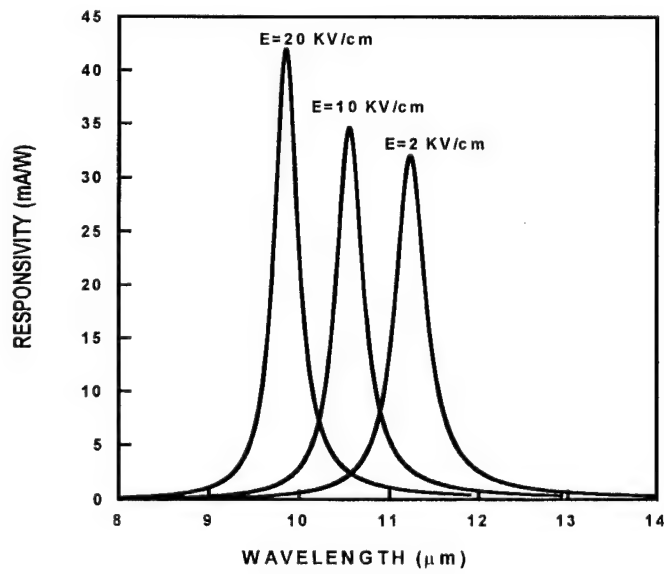


Figure 6.10 Calculated responsivity of the double quantum well QWIP structure under different biases.

## 7. Publications and technical reports

1. Sheng S. Li and Xudong Jiang, *Semi-annual Progress Report*, Army Research Office, Dec. 31, 1997. 46 pages.
2. M. Z. Tidrow, Xudong Jiang, J. C. Chiang, Sheng S. Li and S. W. Kennerly, "Normal Incidence n-Type Direct Gap Quantum Well Infrared Photodetectors," *Proc. of the 5<sup>th</sup> International Symposium on Long Wavelength Infrared Detectors and Arrays*, ECS PV-97-33, edited by S. Li, M. Tidrow, and H.C. Liu, pp.199-208, Sept. 4-6, 1997.
3. M. Z. Tidrow, S. W. Kennerly, Xudong Jiang, J. C. Chiang, Sheng S. Li and V. Ryzhii, "Intersubband Transitions of Normal Incidence N-type Direct Gap Quantum Well Structures," invited talk, *1997 International Conference on Intersubband Transitions in Quantum Wells: Physics and Devices*, Tianan, Taiwan, Dec.15-18, 1997. Paper published in Proc. book volume edited by Sheng S. Li and Y. K. Su, Kluwer Academic Publishers, pp.68-76, June 1998.
4. Xudong Jiang, M.Z. Tidrow and Sheng S. Li, "Investigation of in-plane transition in N-Type Direct Gap QWIPs," to be published in *Journal of Applied Physics*, 1998.
5. M. Z. Tidrow, Xudong Jiang, Sheng S. Li, and K. Bacher "A Novel Four-Color Quantum Well Infrared Photodetector," submitted to *Appl. Phys. Lett.*, June, 1998.
6. M. Z. Tidrow<sup>a</sup>, D. Beekman, S. Kennerly, X. D. Jiang, S. S. Li, A. Singh, and M. Dodd, "Simplified QWIPs for Low Temperature and Low Background Applications," paper presented at 1998 SPIE International Conference on Detectors and Focal Plane Arrays VI, Orlando, FL, April 14-16, 1998. Full paper to be published in Conf. Proceedings.
7. M. Z. Tidrow, Xudong Jiang, Sheng S. Li, and K. Bacher, "A Novel Four-Color Quantum Well Infrared Photodetector," invited talk, *6th International Symposium on Long Wavelength Infrared Detectors and Arrays*, Boston, Nov. 5-6, 1998.
8. Xudong Jiang, M.Z. Tidrow and Sheng S. Li, "A Study of the Quantum Confined Stark Effect in an Asymmetric Weakly Coupled double Quantum Wells Structure", to be published in *Superlattices and Microstructures*, 1998.



## 8. References

1. L.C. West and S.J. Eglash, Appl. Phys. Lett. **46**, 1156 (1985).
2. B.F. Levine, K.K. Choi, C.G. Bethea, J. Walker and R.J. Malik, Appl. Phys. Lett. **50**, 1092 (1987).
3. B.F. Levine, J. Appl. Phys. **74**, R1 (1993).
4. S.D. Gunapala and K.M.S.V. Bandara, Thin Films **21**, 113 (1995).
5. Sheng S. Li, Journal of the Chinese Institute of Electrical Engineering **2**, 37 (1995).
6. Yia-Chung Chang and R.B. James, Phys. Rev. B **39**, 12672 (1989).
7. B.F. Levine, S.D. Gunapala, J.M. Kuo, S.S. Pei and S. Hui, Appl. Phys. Lett. **59**, 1864 (1991).
8. J. Katz, Y. Zhang and W.I. Wang, Electron. Lett. **28**, 932 (1992).
9. C.L. Yang, D.S. Pan and R. Somoano, J. Appl. Phys. **65**, 3253 (1989).
10. L.A. Samoska, B. Brar and H. Kroemer, Appl. Phys. Lett. **62**, 2539 (1993).
11. Y. Zhang, N. Baruch and W.I. Wang, Appl. Phys. Lett. **63**, 1068 (1993).
12. L.S. Yu, S.S. Li and P. Ho, Electron. Lett. **28**, 1468 (1992).
13. L.H. Peng, J.H. Smet, T.P.E. Broekaert and C.G. Fonstad, Appl. Phys. Lett. **61**, 2078 (1992).
14. L.H. Peng, J.H. Smet, T.P.E. Broekaert and C.G. Fonstad, Appl. Phys. Lett. **62**, 2413 (1993).
15. H.S. Li, R.P.G. Karunasiri, Y.W. Chen and K.L. Wang, J. Vac. Sci. Technol. B **11**, 922 (1993).

16. Y. Hirayama, J.H. Smet, L.H. Peng, C.G. Fonstad and E.P. Ippen, Appl. Phys. Lett. **63**, 1663 (1993).
17. J.H. Smet, L.H. Peng, Y. Hirayama and C.G. Fonstad, Appl. Phys. Lett. **64**, 986 (1994).
18. G. Karunasiri, J.S. Park, J. Chen, R. Shih, J.F. Scheihing and M.A. Dodd, Appl. Phys. Lett. **67**, 2600 (1995).
19. Z. Yuan, Z. Chen, D. Cui, J. Ma, Q. Hu, J. Zhou and Y. Zhou, Appl. Phys. Lett. **67**, 930 (1995).
20. M.Z. Tidrow, K.K. Choi, A.J. DeAnni, W.H. Chang and S.P. Svensson, Appl. Phys. Lett. **67**, 1800 (1995).
21. M.Z. Tidrow, J.C. Chiang, Sheng S. Li and K. Bacher, Appl. Phys. Lett. **70**, 859 (1997).
22. M. Zaluzny, Thin Solid Films **76**, 307 (1981).
23. A. Shik, Sov. Phys. Semocond. **22**, 1165 (1988).
24. A. Shik, in *"Intersubband Transitions in Quantum Wells"*, edited by E. Rosencher, B. Vintner and B.F. Levine (Plenum, New York, 1992), p. 319.
25. Rui Q. Yang, J.M. Xu and Mark Sweeny, Phys. Rev. **B50**, 7474 (1994).
26. Rui. Q. Yang, Appl. Phys. Lett. **66**, 959 (1995).
27. Rui. Q. Yang, Phys. Rev. **B52**, 11958 (1995).
28. L.H. Peng and C.G. Fonstad, J. Appl. Phys. **77**, 747 (1995).
29. L.C. Lew Yan Voon, M. Willatzen, M. Cardona and L.R. Ram-Mohan, J. Appl. Phys. **80**, 600 (1996).

30. L.C. Lew Yan Voon, M. Willatzen and L.R. Ram-Mohan, J. Appl. Phys. **78**, 295(1995).
31. S.Y. Wang and C.P. Lee, Appl. Phys. Lett. **71**, 119 (1997).
32. Landolt-Börnstein, *Numerical Data and Functional Relationships in Science and Technology*, O. Madelung, Ed., (Springer-Verlag, Berlin), vols. 17a and 22a (1986).
33. M. Sugawara, N. Okazaki, T. Fujii and S. Yamazaki, Phys. Rev. B **48**, 8102 (1994).
34. V. Ryzhii (private communication).
35. S.Y. Wang and C.P. Lee, J. Appl. Phys. **82**, 2680 (1997).
36. M.Z. Tidrow and K. Bacher, Appl. Phys. Lett. **69**, 3396 (1996).
37. M.Z. Tidrow, K.K. Choi, C.Y. Lee, W.H. Chang, F.J. Towner and J.S. Ahearn, Appl. Phys. Lett. **64**, 1268 (1994).
38. J.C. Chiang, Sheng S. Li, M.Z. Tidrow, P. Ho, M. Tsai and C.P. Lee, Appl. Phys. Lett. **69**, 2412 (1996).
39. A. Hawit and J.S. Harris, Jr., Appl. Phys. Lett. **50**, 685 (1987).
40. D. Ahn, IEEE J. Quantum Electron. **QE-25**, 2260 (1989).
41. Y.J. Mii, R.P.G. Karunasiri, K.L. Wang, M.Chen and P.F. Yuh, Appl. Phys. Lett. **56**, 1986 (1990).
42. Y.H. Wang and S.S. Li, Appl. Phys. Lett. **62**, 621 (1993).
43. Y. Huang, C. Lien and T.F. Lei, J. Appl. Phys. **74**, 2598 (1993).
44. F. Capasso, C. Sirtori and A.Y. Cho, IEEE J. Quantum Electron. **QE-30**, 1313 (1994).
45. T.K. Woodward, J.E. Cunningham and W.Y. Jan, J. Appl. Phys. **78**, 1411 (1995).

46. X.B. Mei, W.G. Bi, C.W. Tu, L.J. Chou, K.C. Hsieh, J. Vac. Sci. Technol. **B14**, 2327 (1996).
47. P. Steinmann, B. Borchert and B. Stegmüller, IEEE Photonics Technology Letters **9**, 191 (1997).
48. "*Handbook of Mathematical Functions*", edited by M. Abramowitz and I.A. Stegun (National Bureau of Standards, Washington D. C., 1964).
49. K.M.S.V. Bandara, D.D. Coon, Byungsung O, Y.F. Lin and M.H. Francombe, Appl. Phys. Lett. **53**, 1931 (1988).